N87-26000

DEVELOPMENT AND APPLICATION OF UNIFIED ALGORITHMS FOR PROBLEMS IN COMPUTATIONAL SCIENCE

Vijaya Shankar and Sukumar Chakravarthy
Rockwell International Science Center

ABSTRACT

This paper presents a framework for developing computationally unified numerical algorithms for solving nonlinear equations that arise in modeling various problems in mathematical physics. The concept of computational unification is an attempt to encompass efficient solution procedures for computing various nonlinear phenomena that may occur in a given problem. For example, in Computational Fluid Dynamics (CFD), a unified algorithm will be one that allows for solutions to subsonic (elliptic), transonic (mixed elliptic-hyperbolic), and supersonic (hyperbolic) flows for both steady and unsteady problems. The objective of the work reported in this paper is manyfold: 1) development of superior unified algorithms emphasizing accuracy and efficiency aspects; 2) development of codes based on selected algorithms leading to validation; 3) application of mature codes to realistic problems; and 4) extension/application of CFD-based algorithms to problems in other areas of mathematical physics. The ultimate objective is to achieve integration of multidisciplinary technologies (stealth, propulsion, aeroelasticity, $\cdots$) to enhance synergism in the design process through computational simulation.

The paper presents specific unified algorithms for a hierarchy of gasdynamic equations (full potential, Euler, and Navier-Stokes) and their applications to a wide variety of problems. Also included are extensions of the CFD methods to two other areas: 1) electromagnetic scattering, and 2) laser-material interaction accounting for melting.

INTRODUCTION

Along with rapid strides in algorithm and code development, the increasing power of super-minicomputers, supercomputers, and graphics workstations is rapidly advancing the state of the art of computational simulation of problems in mathematical physics. One area that is setting the pace is Computational Fluid Dynamics. Other disciplines such as electromagnetic scattering, semiconductor device/process modeling, material characterization, etc., are starting to benefit from the CFD experience.

Modern vehicle concepts such as the Advanced Tactical Fighter (ATF) attempt an effective compromise between the transonic maneuver and supersonic cruise conditions. Multiple design considerations of this type impose stringent constraints on the aerodynamic shape of the vehicle to achieve high buffet-free lift performance with reduced trim drag. The recent resurgence of the hypersonics program through the National Aerospace Plane (NASP) project also demands analysis and design of vehicles with requirements to fly through the entire Mach number range (subsonic to hypersonic) requiring increasingly sophisticated nonlinear methods to better understand various gasdynamic flow processes.

The Navier-Stokes equations best represent the physics of nonlinear flow. However, limitations in memory and execution speed of present-day supercomputers restrict the routine use of Navier-Stokes methods. For wider application of CFD in the aerospace industry, cost-effective methods based on less exact forms of gasdynamic equations, such as the Euler and full potential equations, are still attractive. The objective of the work reported in this paper is to develop, for all speed regimes, efficient, accurate, and robust nonlinear methods for equations ranging from the simple full potential to the complex Navier-Stokes. Development of such a spectrum of hierarchical capability is critical for efficient and cost-effective design of aerospace configurations. The general philosophy of numerical design through progression of increasingly sophisticated nonlinear tools is illustrated in figure 1, and represents a summary of the numerical design experience at Rockwell covering the HiMAT, forward swept wing, SAAB, and Air Force/Navy Research Technology contract studies[1-4].

Referring to figure 1, in designing a configuration, linear theory[5,6] is first used to establish candidate optimum thickness, twist, camber, and variable camber deflections at supersonic speeds. Second, nonlinear methods (full potential and Euler) are employed to capture embedded shock waves at transonic[7-14] and supersonic[15-21] conditions and weaken the wave system through parametric redesign. Boundary layer analysis[22] and Navier-Stokes codes[23-26] are subsequently used to assess the flow quality of the nonlinear inviscid design. The extent of separation in particular is evaluated, and a subsequent redesign is performed to minimize its extent.
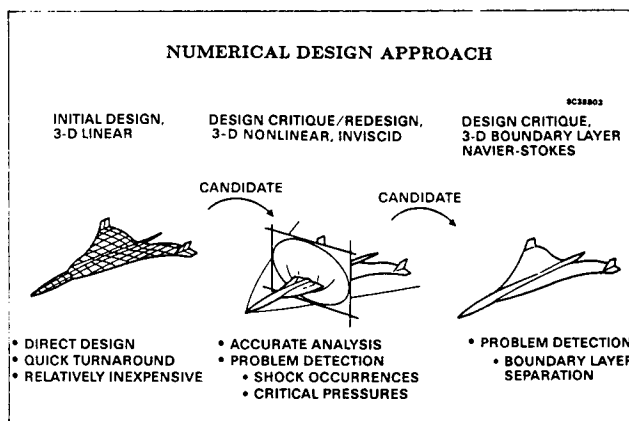

Fig. 1. Progression of improved design through nonlinear analysis.

PRECEDING PAGE BLANK NOT FILMED

At Rockwell, the computational activity is carried out on several fronts. 1) Algorithm development. Under this task, several algorithmic issues such as higher order space/time accuracy, efficiency, multizone gridding concepts, multigrid cycling, upwind total variation diminishing (TVD) schemes, vectorization concepts, implicit/explicit methods, etc., are stressed. The primary thrust of this activity is computational unification of methodologies encompassing efficient solution procedures for computing various flow phenomena occurring across the Mach number range. 2) Code development. Under this task, selected algorithms (based on the study from task 1)) with potential to mature into a production code capability are further developed and undergo extensive validation. Some of the issues stressed in this phase are computational efficiency through code vectorization, user orientation/documentation, code transportability, graphics interface, and user training. 3) Application. At this stage, codes from task 2) that have matured into a production code with established user confidence, are applied to study a wide range of realistic problems to better understand flows over existing configurations (Shuttle Orbiter, B-1B, etc.) as well as to design aerospace configurations for the next generation (ATF, NASP, Transatmospheric Vehicles (TAV), etc.). 4) Extension of CFD methods to non-CFD problems. Under this task, a host of problem areas in mathematical physics that are governed by appropriate partial differential equations is dealt with. The techniques developed for studying problems in Computational Fluid Dynamics are well suited for studying problems in electromagnetic scattering, laser-material interaction, and semiconductor device/process modeling, just to name a few.

Computational Fluid Dynamics is rapidly advancing. Its methods are beginning to influence how problems are and can be effectively solved in other disciplines. As this process of spreading the wealth of CFD knowledge to other areas continues, the CFD discipline is expected to play a key role in the future, together with state-of-the-art computers, in integrating multidisciplinary technologies to enhance synergism in the design process through computational simulation.

The paper presents a brief summary of some of the unified algorithms developed for various gasdynamic equations, along with their applications to many fluid dynamic problems. Also presented are some applications of CFD methods to non-fluid dynamic problems. More details on the algorithmic aspects of the unified concept can be found in the references.

This paper represents a collection of work performed by many researchers in the Computational Fluid Dynamics Department at Rockwell International Science Center.

EQUATIONS IN CONSERVATION FORM

For many problems in mathematical physics, the physical process to be modeled is governed by an appropriate set of linear or nonlinear partial differential equations. For example, many fluid dynamic processes are governed by the Navier-Stokes equations, the electromagnetic scattering from objects is modeled by Maxwell's equations[27], and problems in semiconductors are governed by Van Roos-broeck[28] equations involving the nonlinear coupling between the electrostatic potential and the electron/hole density.

In general, many of these equations naturally lend themselves to a conservation form representation given by

$$Q_t + E_x + F_y + G_z = 0 \tag{1}$$

where the dependent variable vector Q, and the fluxes E, F, and G take on different forms depending on the equation being modeled. The form of Q, E, F, and G for the full potential, Euler, Navier-Stokes, and the Maxwell equations are presented in the subsequent sections. Application of eq. (1) to many realistic problems requires a coordinate transformation to properly represent the physical domain of interest and to aid in the boundary condition treatment.

Under the transformation of coordinates implied by

$$\tau = t, \xi = \xi(t,x,y,z), \eta = \eta(t,x,y,z), \varsigma = \varsigma(t,x,y,z),$$

eq. 1 can be recast in the conservation form given by

$$\overline{Q}_\tau + \overline{E}_\xi + \overline{F}_\eta + \overline{G}_\varsigma = 0 \quad , \tag{2a}$$

where

$$\overline{Q} = \frac{Q}{J} \quad ,$$

$$\overline{E} = \frac{\xi_t}{J}Q + \frac{\xi_x}{J}E + \frac{\xi_y}{J}F + \frac{\xi_z}{J}G \quad ,$$

$$\overline{F} = \frac{\eta_t}{J}Q + \frac{\eta_x}{J}E + \frac{\eta_y}{J}F + \frac{\eta_z}{J}G \quad , \tag{2b}$$

$$\overline{G} = \frac{\varsigma_t}{J}Q + \frac{\varsigma_x}{J}E + \frac{\varsigma_y}{J}F + \frac{\varsigma_z}{J}G \quad .$$

where, in turn, J is the Jacobian of the transformation

$$J = \partial(\xi,\eta,\varsigma)/\partial(x,y,z) \tag{2c}$$

and

$$\xi_t = -(\xi_x x_\tau + \xi_y y_\tau + \xi_z z_\tau)$$
$$\eta_t = -(\eta_x x_\tau + \eta_y y_\tau + \eta_z z_\tau) \tag{2d}$$
$$\varsigma_t = -(\varsigma_x x_\tau + \varsigma_y y_\tau + \varsigma_z z_\tau) \quad .$$

Associating the subscripts j,k,l with the ξ,η,ς directions, a numerical approximation to eq. (2a) may be expressed in the semi-discrete conservation law form given by

$$(\widehat{Q}_{j,k,l})_\tau + (\widehat{E}_{j+1/2,k,l} - \widehat{E}_{j-1/2,k,l})$$
$$+ (\widehat{F}_{j,k+1/2,l} - \widehat{F}_{j,k-1/2,l}) \tag{3}$$
$$+ (\widehat{G}_{j,k,l+1/2} - \widehat{G}_{j,k,l-1/2}) = 0$$

where $\widehat{E}, \widehat{F}, \widehat{G}$ are numerical or representative fluxes at the bounding sides of the cell for which discrete conservation is considered, and $\widehat{Q}_{j,k,l}$ is the representative conserved quantity (the numerical approximation to $\overline{Q}$) considered conveniently to be the centroidal value. The half-integer subscripts denote cell sides and the integer subscripts the cell itself or its centroid.

The semi-discrete conservation law given by eq. (3) may be regarded as representing a finite volume discretization if the following associations are made:

$$\widehat{Q}_{j,k,l} = Q V_{j,k,l} \qquad (4a)$$

where V is the volume of the cell under consideration;

$$\left(\frac{\xi_{x,y,z}}{J}\right)_{j\pm 1/2} =$$

$$n_{x,y,z}\{(k-1/2, l-1/2), (k+1/2, l-1/2),$$
$$(k+1/2, l+1/2), (k-1/2, l+1/2)\}_{j\pm 1/2} \quad ,$$

$$\left(\frac{\eta_{x,y,z}}{J}\right)_{k\pm 1/2} =$$

$$n_{x,y,z}\{(j-1/2, l-1/2), (j-1/2, l+1/2),$$
$$(j+1/2, l+1/2), (j+1/2, l-1/2)\}_{k\pm 1/2} \quad ,$$

$$\left(\frac{\varsigma_{x,y,z}}{J}\right)_{l\pm 1/2} =$$

$$n_{x,y,z}\{(j-1/2, k-1/2), (j+1/2, k-1/2),$$
$$(j+1/2, k+1/2), (j-1/2, k+1/2)\}_{l\pm 1/2} \quad ; \qquad (4b)$$

$$\left(\frac{\xi_t}{J}\right)_{j\pm 1/2} = -\,(\frac{\xi_x}{J})_{j\pm 1/2}(x_\tau)_{j\pm 1/2}$$
$$-(\frac{\xi_y}{J})_{j\pm 1/2}(y_\tau)_{j\pm 1/2} - (\frac{\xi_z}{J})_{j\pm 1/2}(z_\tau)_{j\pm 1/2}$$

$$\left(\frac{\eta_t}{J}\right)_{k\pm 1/2} = -\,(\frac{\eta_x}{J})_{k\pm 1/2}(x_\tau)_{k\pm 1/2}$$
$$-(\frac{\eta_y}{J})_{k\pm 1/2}(y_\tau)_{k\pm 1/2} - (\frac{\eta_z}{J})_{k\pm 1/2}(z_\tau)_{k\pm 1/2} \qquad (4c)$$

$$\left(\frac{\varsigma_t}{J}\right)_{l\pm 1/2} = -\,(\frac{\varsigma_x}{J})_{l\pm 1/2}(x_\tau)_{l\pm 1/2}$$
$$-(\frac{\varsigma_y}{J})_{l\pm 1/2}(y_\tau)_{l\pm 1/2} - (\frac{\varsigma_z}{J})_{l\pm 1/2}(z_\tau)_{l\pm 1/2}$$

In the above, $n_{x,y,z}$ are the x, y, z components of the representative normals to the surface formed by the four points a, b, c, d implied in $n_{x,y,z}(a, b, c, d)$. These four points are not necessarily coplanar. Also, $(x_\tau, y_\tau, z_\tau)_{j\pm 1/2, k\pm 1/2, l\pm 1/2}$ are the x, y, z components of the appropriate cell-face representative velocities. These describe the motion of the cell face and will be zero for a stationary grid. In the following, we can use the notation n_t to describe the representative cell-face normal velocities:

$$(n_t)_{j\pm 1/2} = \left(\frac{\xi_t}{J}\right)_{j\pm 1/2}$$
$$(n_t)_{k\pm 1/2} = \left(\frac{\eta_t}{J}\right)_{k\pm 1/2} \qquad (4d)$$
$$(n_t)_{l\pm 1/2} = \left(\frac{\varsigma_t}{J}\right)_{l\pm 1/2}$$

The evaluation of the volume, cell-face normals and cell-face normal velocities (metrics) are presented in Ref. 14.

Within this framework of a finite volume representation, the concept of a unified algorithm/solver addresses two issues: 1) representation of the numerical fluxes $\widehat{E}, \widehat{F}$, and $\widehat{G}$ to account for different physical phenomena to be encountered in the problem being modeled (for example, in fluid dynamics, a unified flux representation will allow for

subsonic, transonic, and supersonic flow situations for both steady and unsteady, including proper transition through shocks and sonic rarefaction); and 2) numerical issues of solving eq. (3). Under the numerical issue, a unified algorithm will be one that performs both the space and time integration within the logic of a single solver. A unified solution treatment will allow one to consider a wide class of problem areas within the capability of a single code. For example, in fluid dynamics, a unified solver will perform space marching for supersonic flows (supersonic flow direction is treated as time like) and allow time marching for subsonic, transonic, and unsteady flows.

The objective is to solve eq. (3) for the dependent vector Q. After incorporation of proper flux representation, the discrete form of eq. (3) can be written as

$$R(Q) = 0. \qquad (5)$$

If Q is known at a known neighborhood state, denoted by Q^*, then solution to eq. (5) can be written as

$$\frac{\partial R}{\partial Q}(Q - Q^*) = -R(Q^*) \qquad (6)$$

where $\frac{\partial R}{\partial Q}$, in general, is a differential operator. Many numerical algorithmic issues such as implicit, explicit, relaxation, approximate factorization, algorithm unification, etc., come into play in the modeling of the differential operator $\frac{\partial R}{\partial Q}$. Issues such as higher order accuracy, proper upwinding, etc., come into $\frac{\partial R}{\partial Q}$ as well as in the modeling of the right hand side $R(Q^*)$. For a unified code that accounts for both space and time marching, one option is to split the $\frac{\partial R}{\partial Q}$ operator in the form

$$\frac{\partial R}{\partial Q} = L_\eta L_\varsigma \qquad (7)$$

where

$$L_\eta = L_\eta[(\tau, \xi), \eta] \quad , \quad L_\varsigma = L_\varsigma[(\tau, \xi), \varsigma].$$

Equation (7) represents a double approximate factorization in the (η, ς) plane with relaxation in the ξ-direction assumed to represent the predominant flow direction. The grouping (τ, ξ) in the L_η and L_ς operator represents a collection of terms involving time and ξ derivative terms. For time marching, the time–step–size $\Delta\tau$ is chosen to maintain the stability and accuracy of the operator, eq. (7). For space marching, $\Delta\tau$ is usually set very large and the operator L_η becomes $L_\eta(\xi, \eta)$ and $L_\varsigma = L_\varsigma(\xi, \varsigma)$ representing ξ as the marching direction. Space marching along ξ is possible only if the equation is hyperbolic with respect to that direction. A code that is based on the unified solver will include the following options:

$$\frac{\partial R}{\partial Q} = L_\varsigma(\varsigma, \tau) L_\eta(\eta, \tau) L_\xi(\xi, \tau) \quad - \text{ Triple approximate factorization with time marching} \qquad (8a)$$

$$\frac{\partial R}{\partial Q} = L_\eta[(\tau, \xi), \eta] L_\varsigma[(\tau, \xi), \varsigma] \quad - \text{ Double approximate factorization with time marching} \qquad (8b)$$

89

$$\frac{\partial R}{\partial Q} = L_\eta(\xi,\eta)L_\varsigma(\xi,\eta)$$

- Space marching
along ξ setting (8c)
$\Delta\tau \to \infty$.

If one employs an upwind differencing, $\frac{\partial R}{\partial Q}$ can also be represented by a Gauss–Siedel relaxation maintaining diagonal dominance. More discussions on these ideas can be found in Refs. 12, 19, and 20.

For time marching, Q^* is usually set to be Q^n as a first guess where Q^n is the solution at the previous time plane. For space marching, Q^* is initially set to be Q_{j-1} representing the solution at the previous space marching plane in the ξ direction. Starting from the initial guess for Q^*, eq. (6) is iterated to convergence driving $\| Q - Q^* \|$ to some preset small value at every time or space marching plane. Usually, this process might involve only a few iterations.

The issue of numerical flux representation is dealt with in the subsequent sections for a variety of equations, namely 1) full potential, 2) Euler, 3) Navier–Stokes, 4) Maxwell, and 5) incompressible Navier–Stokes, representing the laser–material interaction.

Full Potential Equation

The full potential equation represents the inviscid, irrotational, and isentropic flow. In spite of these assumptions, this form of the gasdynamic equation is widely in use for analyzing complex configurations at transonic and low supersonic Mach numbers. As long as the shocks are weak (Mach number normal to a shock surface less than 1.3 to 1.5), the full potential isentropic shocks will be in agreement with the Rankine–Hugoniot jump conditions.

Referring to eq. (1), the full potential equation takes the form $Q = \rho$, $E = \rho u$, $F = \rho v$, and $G = \rho w$, where ρ is the density and u, v, and w are the Cartesian velocities. All the quantities ρ, u, v, and w are expressible in terms of a single scalar function ϕ, the velocity potential. Using Bernoulli's law, the density ρ is given by

$$\rho^{\gamma-1} = 1 - \frac{\gamma-1}{2}M_\infty^2 \left[2\phi_\tau + (U + \xi_t)\phi\xi \right. \\ \left. + (V + \eta_t)\phi_\eta + (W + \varsigma_t)\phi_\varsigma - 1 \right] \tag{9}$$

and U, V, and W are the contravariant velocities.

Referring to eq. (3), modeling of the time term $\widehat{Q}_\tau$ will require time linearization for density to express ΔQ in terms of $\Delta\phi = \phi - \phi^*$. The density linearization is given by

$$\rho = \rho(\phi_*) + \left(\frac{\partial\rho}{\partial\phi}\right)_{\phi=\phi_*} \Delta\phi \tag{10}$$

where

$$\left(\frac{\partial\rho}{\partial\phi}\right)_{\phi=\phi_*} = \left[-\frac{\rho}{a^2}\left\{ \frac{1}{\Delta\tau_1} + U\frac{\partial}{\partial\xi} + V\frac{\partial}{\partial\eta} + W\frac{\partial}{\partial\varsigma} \right\} \right]_{\phi=\phi_*} \tag{11}$$

is a differential operator.

Equation (3) also requires evaluation of $\widehat{E}$, $\widehat{F}$, and $\widehat{G}$ at various spatial half node points. As mentioned earlier, $\widehat{E}$ represents $\overline{E}$ appearing in eq. (2a).

The concept of developing a unified full potential scheme stems from a proper definition for the numerical or representative fluxes $\widehat{E}$, $\widehat{F}$, $\widehat{G}$ at cell interfaces derived from the theory of characteristic signal propagation. Depending on the type of flow at the cell interface (subsonic, transonic, or supersonic), the fluxes are properly defined employing an upwind bias to eliminate numerical or spurious (unphysical) oscillations by satisfying entropy conditions (no expansion shocks).

Based on the characteristic system at a cell interface in the time–space domain, the following different flux representations are made.

Subsonic at cell face $j + 1/2$ $\left(U < c\sqrt{a_{11}}\right)$

$$\widehat{E}_{j+1/2} = \overline{E}_{j+1/2} \qquad \text{(zero biasing)}$$

Transonic at $j + 1/2$ $\left(U < c\sqrt{a_{11}}\ ,\quad q > c\right)$

$$\widehat{E}_{j+1/2} = \widetilde{\overline{E}}_{j+1/2} \qquad \text{(to be defined later)} \tag{12}$$

Supersonic at $j + 1/2$ $\left(U > c\sqrt{a_{11}}\right)$

$$\widehat{E}_{j+1/2} = \overline{E}_{j-1/2} \qquad \text{(upwind biased flux)}$$

In eq. (12), c is the speed of sound and $a_{11} = \left(\xi_x^2 + \xi_y^2 + \xi_z^2\right)$. The transonic flux $\widetilde{\overline{E}}$ is defined in terms of an upwind biased density based on flux biasing. Define

$$\tilde{\rho} = \frac{1}{q}\left[(\rho q) \pm \left\{ \frac{U}{Q}\frac{\partial}{\partial\xi} + \frac{V}{Q}\frac{\partial}{\partial\eta} + \frac{W}{Q}\frac{\partial}{\partial\varsigma} \right\}(\rho q)^- \right] \tag{13}$$

where $Q = \sqrt{U^2 + V^2 + W^2}$.

The quantity $(\rho q)^-$ appearing in eq. (13) is defined to be

$$\begin{aligned} (\rho q)^- &= \rho q - \rho^* q^* \quad &\text{if } q > q^* \\ &= 0 \quad &\text{if } q \le q^* \end{aligned} \tag{14}$$

The quantities $\rho^* q^*$, ρ^*, and q^* represent sonic values of the flux, density, and total velocity, respectively. These sonic conditions are given by (using the density and speed of sound relationships)

$$\left(q^*\right)^2 = \frac{1 + \frac{(\gamma-1)}{2}M_\infty^2\left(1 - 2\phi_\tau - 2\varsigma_t\phi_\varsigma - 2\eta_t\phi_\eta - 2\xi_t\phi_\xi\right)}{\frac{\gamma+1}{2}M_\infty^2}$$

$$\rho^* = \left(q^* M_\infty\right)^{2/(\gamma-1)}. \tag{15}$$

Note that for steady flows, the sonic conditions ρ^* and q^* are only a function of the freestream Mach number, and for a given flow they are constants. For unsteady flows, ρ^* and q^* need to be computed everywhere due to the presence of ϕ_τ and other unsteady terms in eq. (15).

In the final discretized form, the full potential equation is written in the form of eq. (6) with $\Delta\phi = (\phi - \phi^*)$ as a single unknown at a grid point.

Some results are presented to illustrate the unified full potential capability in computing subsonic, transonic, and supersonic steady/unsteady flows.

Full Potential Results

Supersonic Flows — Supersonic flows are computed using the marching option within the unified solver.

Figure 2 shows the surface gridding along with cross-plane field grid points for a typical advanced generic fighter. The body–fitted grid is generated at every marching plane using standard elliptic grid solvers. Figure 3 shows pressure contours at two different axial stations at $M_\infty = 1.6$, $\alpha = 4.94°$. The crossplane geometry in figure 3 clearly shows the fuselage, vertical tail, wing, and the flow through nacelle along with the wake cut behind the trailing edge of the wing. Figure 4 shows pressure correlation between the computations and experimental data at two different span stations. Table 1 gives correlations for overall force and moment coefficients for different angles of attack and side slip angles. The impact of CFD on the development of advanced configurations is illustrated in figure 5. It shows the L/D performance for the configuration of figure 2 for across the Mach number range and compares that performance with existing fighters such as the F-14 and the F-15. A 25% to 50% increase in L/D is demonstrated.

Figure 6 shows a complex fighter configuration with canard, wing, vertical tail, swept–side–walled flow through nacelle, and a canopy. The gridding at different axial stations is shown. Figure 7 shows the pressure contours at different marching planes at $M_\infty = 2.0$, $\alpha = 4°$. A comparison of overall force and moment coefficients is given in Table 2. Figure 6 illustrates the extent of geometric complexity that can be handled by the full potential code for supersonic flows. However, for transonic and subsonic flows where the computational domain has to extend far upstream and far downstream of the configuration, the requirement for a global three–dimensional grid makes treatment of complex configurations more formidable.
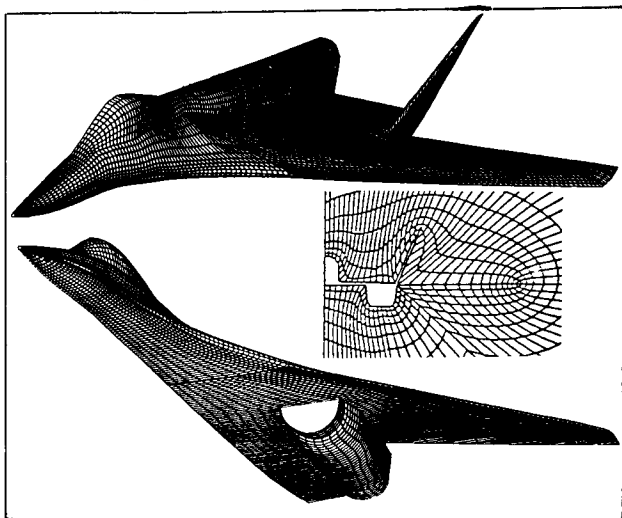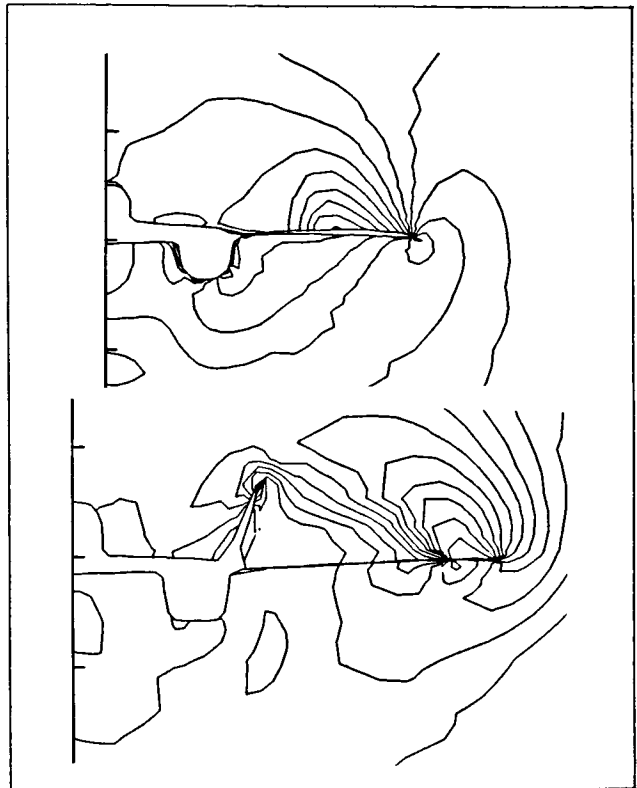

Fig. 2. Computational grid for a fighter.

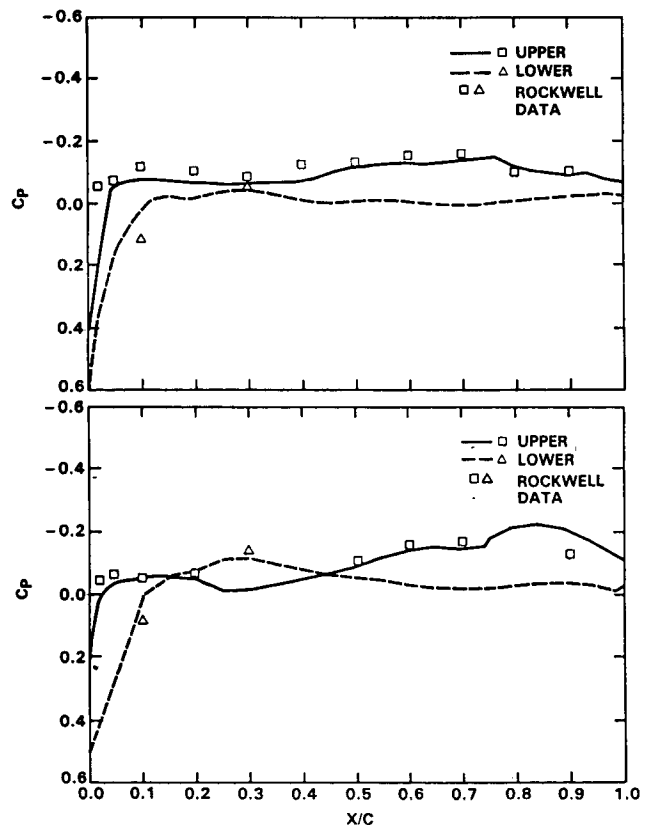Fig. 3. Pressure contours at two different axial stations.

Fig. 4. Chordwise pressure distribution at 60% and 80% span stations; $M_\infty = 1.6$, $\alpha = 1.24°$.

91

$C - 2$

	β = 0°				β = 4.0°	
α	1.24		4.94		6.0°	
M_∞	1.6		1.6		1.6	
	F.P.	Data	F.P.	Data	F.P.	Data
C_L	0.119	0.105	0.3058	0.303	0.37	0.40
C_D	0.0293	0.0280	0.0455	0.0475	0.058	0.053
C_Y	0	0	0	0	-0.0454	0.0380
C_M	-0.0248	-0.021	-0.051	-0.045	-0.0542	-0.075

Table 1. Comparison of force and moment coefficients.
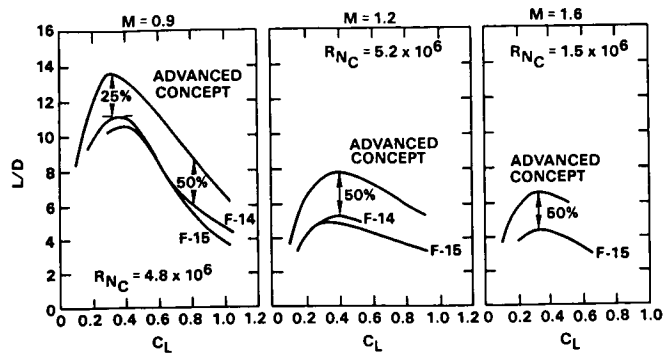
Fig. 5. Impact of CFD on advanced configuration development.
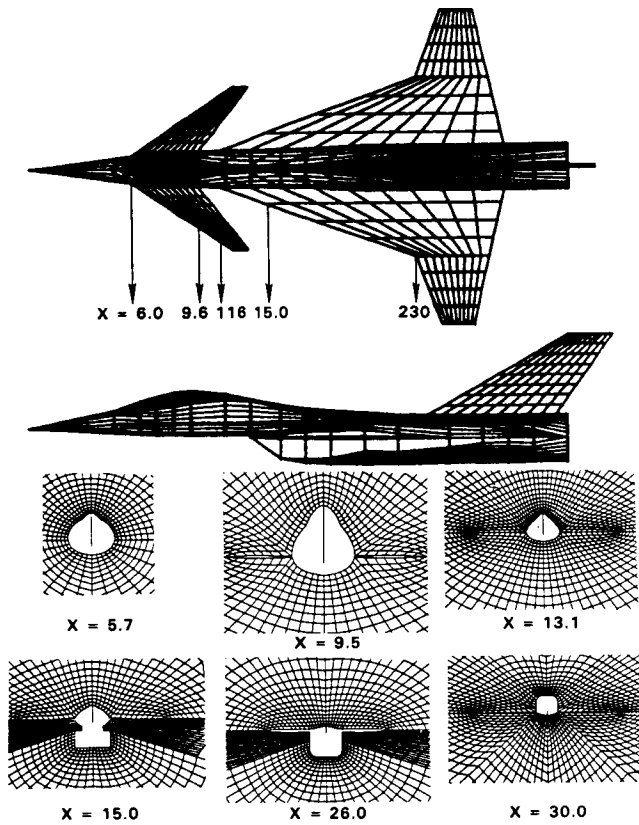
Fig. 6. Modeling of a canard-wing fighter.

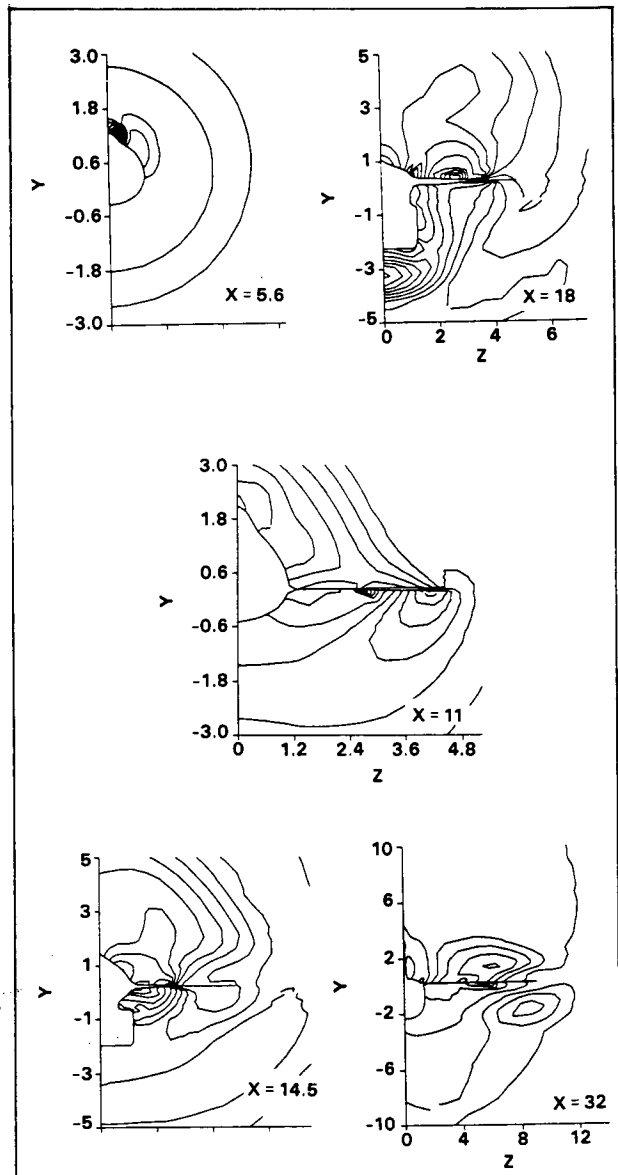|	β = 0		β = 3.18	
α	4.0		3.78	
M_∞	2.0		2.0	
	F.P.	Data	F.P.	Data
C_L	0.151	0.153	0.148	0.153
C_D	0.031	0.0302	0.0306	0.0309
C_Y	0	0	0.0350	0.037
C_M	0.0056	0.0061	0.0071	0.0066

Table 2. Comparison of force and moment coefficients.

Fig. 7. Pressure contours; $M_\infty = 2$, $\alpha = 4°$.

Transonic Flows — Figure 8 shows results for a canard-wing configuration at transonic Mach numbers. A wake cut is created between the trailing edge of the canard and the leading edge of the wing, as well as behind the trailing edge of the wing. For steady transonic computations, triple approximate factored time marching is performed until steady state is reached. A typical computation such as the one shown in figure 8 requires 100 to 200 time iterations requiring 60 seconds of CPU time on a CRAY-X/MP for 80,000 grid points.
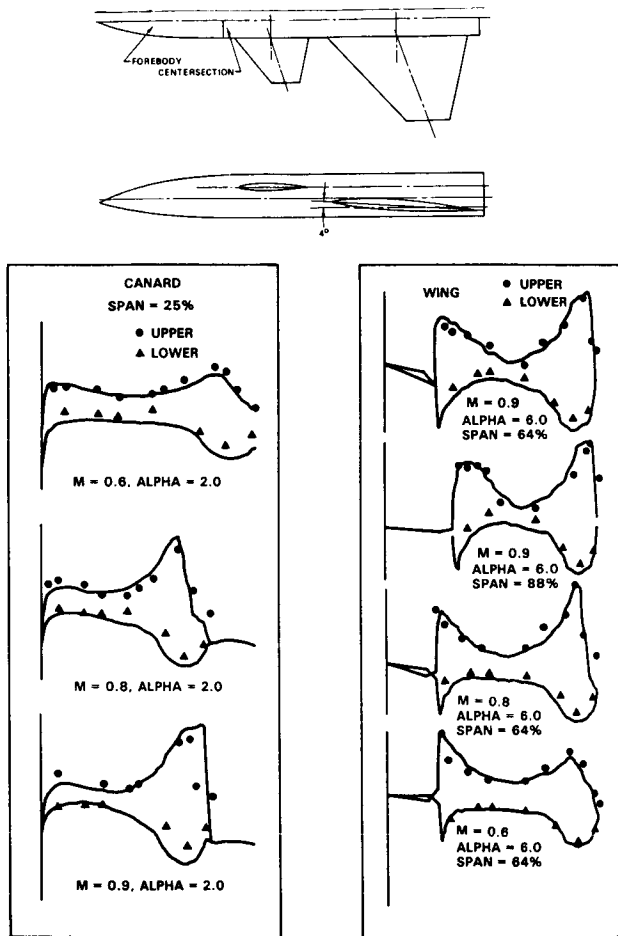
Fig. 8. Pressure correlations for a transonic canard-wing configuration.

Static Aeroelastic — Figure 9 illustrates a static aeroelastic computation for a flexible wing. The structural response is modeled using a generalized modal representation[9]. Within the aeroelastic model, a rigid wing is represented by setting the dynamic pressure to be zero. The magnitude of the structural deflection depends on the level of prescribed dynamic pressure and the generalized mode shapes. For an aeroelastically stable configuration, the tip load is reduced once the wing undergoes static deflection. This is illustrated in figure 9 which shows the deflected wing shape along with the upper and lower surface pressures. Figure 10 shows the C_L versus α variation taking into account static flexibility.
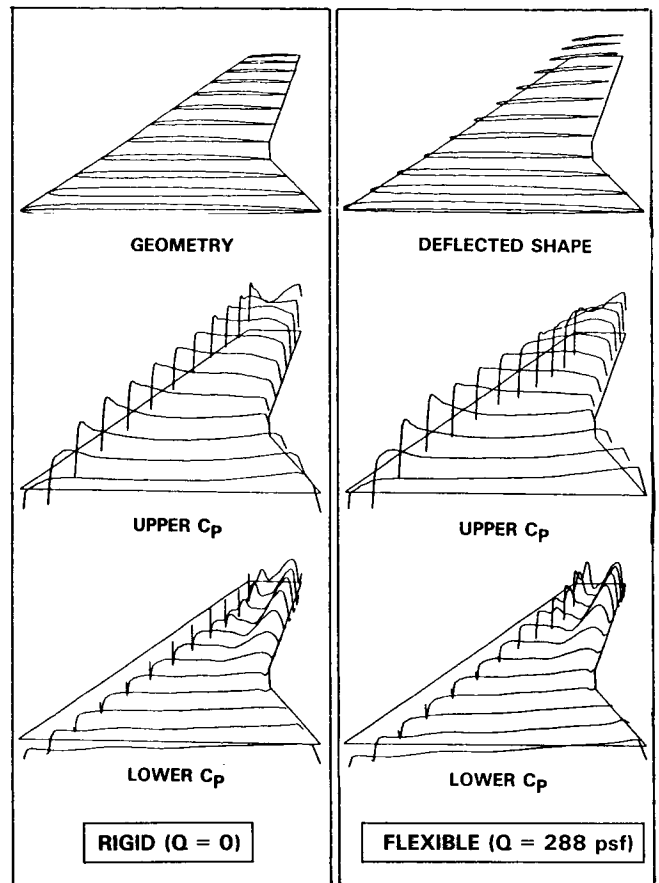
$M_\infty = 1.15$, $\alpha = 6°$
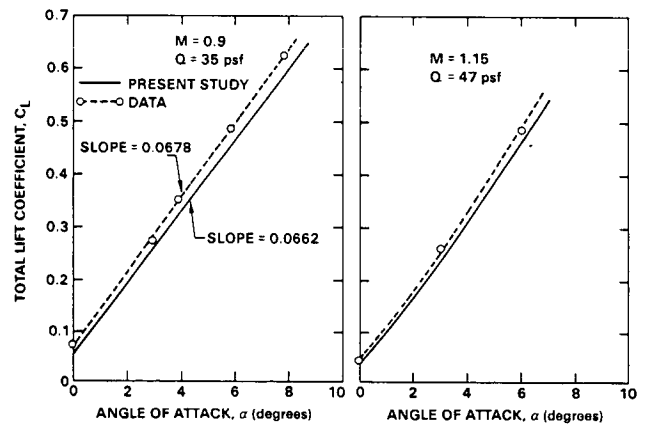

Fig. 9. Static flexible computation.

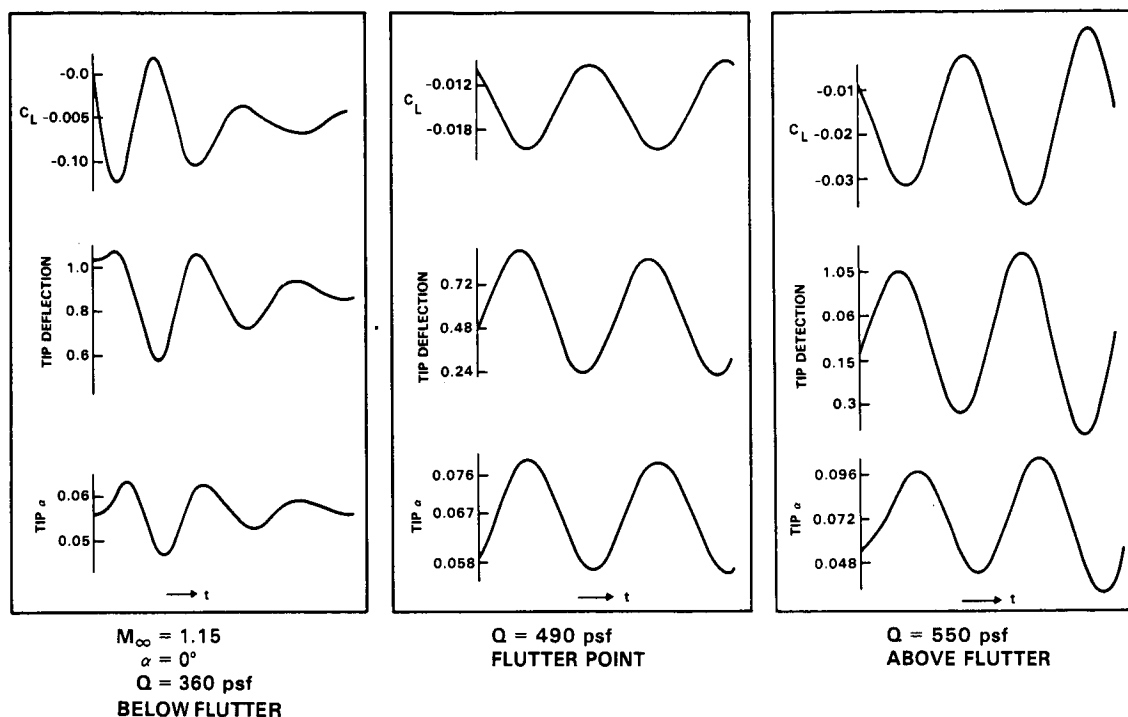Fig. 10. C_L versus α correlation for the flexible wing.

93

Fig. 11. Dynamic flexible computations for different dynamic pressures; a) below flutter, b) at flutter point, and c) above flutter point.

Dynamic Aeroelastic — Figure 11 shows dynamic flexible computations for three different dynamic pressure levels. Dynamic computations are performed as time–dependent calculations coupling the nonlinear aerodynamics and the structural response at a given time level invoking a time–accurate, Newton iteration procedure[9]. For a dynamic pressure level below the flutter point, the wing is aeroelastically stable as indicated by the decaying amplitude of oscillation in C_L, tip deflection, and tip α as a function of time in figure 11a. Figure 11b shows the calculation near flutter point with zero damping of the amplitude while figure 11c shows results of aeroelastic divergence above the flutter point.

Euler Equations

Referring to eq. (1), the Euler equations are given by

$$
Q = \begin{pmatrix} e \\ \rho \\ \rho u \\ \rho v \\ \rho w \end{pmatrix}, E = \begin{pmatrix} (e+p)u \\ \rho u \\ \rho u^2 + p \\ \rho vu \\ \rho wu \end{pmatrix},
$$

$$
F = \begin{pmatrix} (e+p)v \\ \rho v \\ \rho uv \\ \rho v^2 + p \\ \rho wv \end{pmatrix}, G = \begin{pmatrix} (e+p)w \\ \rho w \\ \rho uw \\ \rho vw \\ \rho w^2 + p \end{pmatrix}. \tag{16}
$$

In the above, pressure is p computed from $p = (e - \rho(u^2 + v^2 + w^2)/2))(\gamma - 1)$, density is ρ, Cartesian x, y, z velocity components are u, v, w, and the total energy per unit volume is e.

In order to define the appropriate numerical fluxes $\widehat{E}$, $\widehat{F}$, $\widehat{G}$, an upwind biased scheme based on Roe's approximate Riemann solver[29] is employed.

At every cell interface $m+1/2$, let $Q^+_{m+1/2}$ and $Q^-_{m+1/2}$ denote the values of the dependent variables defined just to the right of and just to the left of the cell face. These values will be defined in the next subsection using a Total Variation Diminishing (TVD) formulation. The Riemann Solver is a mechanism to divide the flux difference between these neighboring states (between $Q^+_{m+1/2}$ and $Q^-_{m+1/2}$) into component parts associated with each wave field. These can in turn be divided into those that correspond to positive and negative wave speeds. When we compute the numerical flux at the cell face at $m + 1/2$, in the finite-volume formulation, we will only use the cell-face normals defined at $m + 1/2$ in the terms contributing to that representative flux. The actual fluxes $\overline{E}, \overline{F}, \overline{G}$, when evaluated with the metrics equated to cell-face normals, can all be written in the same functional form given by

$$
\overline{E}, \overline{F}, \overline{G} = f(Q, n_x, n_y, n_z) = f(Q, N) \tag{17}
$$

where the appropriate values of n_x, n_y, n_z are used and N denotes the set of those normals. Using such notation, it is possible to present the necessary algebra very concisely.

Let us first denote the Jacobian matrix of the flux f with respect to the dependent variables Q by $\partial f/\partial Q$. This Jacobian can also be called the coefficient matrix. Let us denote the eigenvalues of the coefficient matrix by λ^i and the corresponding left and right eigenvectors by ℓ^i and r^i,

94

respectively. The matrix formed by the left eigenvectors as its rows is then called the left eigenvector matrix L and the matrix of right eigenvectors comprising the right eigenvectors as its columns is R. For our purposes, we choose an orthonormal set of left and right eigenvectors which implies that $LR = RL = I$, the identity matrix. In the above, the superscript i has been used to denote the association of the i-th eigenvalue with its corresponding eigenvector. Each eigenvalue is also associated with its own wave field.

The underlying upwind scheme is based upon Roe's approximate Riemann solver. In this approach, cell interface values of density, velocities, and enthalpy ($h = \gamma p/((\gamma - 1)\rho) + (u^2 + v^2 + w^2)/2$) are computed using a special averaging procedure[14].

Knowing the cell interface values, the eigenvalues and orthonormal set of left and right eigenvectors corresponding to a cell face can be computed. These may be denoted by

$$
\begin{aligned}
\lambda^i_{m+1/2} &= \lambda^i_{m+1/2}(Q_{m+1/2}, N_{m+1/2}), \\
\ell^i_{m+1/2} &= \ell^i_{m+1/2}(Q_{m+1/2}, N_{m+1/2}), \\
r^i_{m+1/2} &= r^i_{m+1/2}(Q_{m+1/2}, N_{m+1/2}).
\end{aligned}
\tag{18a}
$$

At each cell face, the positive and negative projections of the eigenvalues may be defined by

$$
\lambda^{i\pm} = \frac{(\lambda^i_{m+1/2} \pm |\lambda^i_{m+1/2}|)}{2} \quad, i = 1, \cdots, 5 \quad.
\tag{18b}
$$

Now, the numerical flux $\widehat{f}_{m+1/2}$ is constructed from

$$
\begin{aligned}
\widehat{f}_{m+1/2} &\\
= \frac{1}{2} &\left[f(Q^+_{m+1/2}, N_{m+1/2}) + f(Q^-_{m+1/2}, N_{m+1/2}) \right] \\
- \frac{1}{2} &\left[\sum_i \left(\lambda^{i+}_{m+1/2} - \lambda^{i-}_{m+1/2} \right) \alpha^i_{m+1/2} r^i_{m+1/2} \right] \\
= f(Q^-_{m+1/2}, N_{m+1/2}) &+ \sum_i \lambda^{i-}_{m+1/2} \alpha^i_{m+1/2} r^i_{m+1/2} \\
= f(Q^+_{m+1/2}, N_{m+1/2}) &- \sum_i \lambda^{i+}_{m+1/2} \alpha^i_{m+1/2} r^i_{m+1/2}
\end{aligned}
\tag{19}
$$

In the above equation,

$$
\alpha^i_{m+1/2} = \ell^i_{m+1/2}(Q^+_{m+1/2} - Q^-_{m+1/2}).
\tag{20}
$$

We can construct upwind-biased schemes of varying accuracies by properly defining the left and right states used in the last subsection. We present here a family of schemes. For use in what follows, let us now define

$$
\begin{aligned}
\widehat{\alpha}^i_{m+1/2} &= \ell^i_m(Q_{m+1} - Q_m), \\
\widehat{\alpha}^i_{m-1/2} &= \ell^i_m(Q_m - Q_{m-1}),
\end{aligned}
\tag{21}
$$

where

$$
\ell^i_m = \ell^i(Q_m, (N_{m+1/2} + N_{m-1/2})/2)
\tag{22}
$$

Next, we define the slope-limited values given by

$$
\begin{aligned}
\widetilde{\alpha}^i_{m+1/2} &= \mathrm{minmod}[\widehat{\alpha}^i_{m+1/2}, b\,\widehat{\alpha}^i_{m-1/2}], \\
\widetilde{\alpha}^i_{m-1/2} &= \mathrm{minmod}[\widehat{\alpha}^i_{m-1/2}, b\,\widehat{\alpha}^i_{m+1/2}].
\end{aligned}
\tag{23}
$$

In the above, the compression parameter b is to be taken as the following function of the accuracy parameter ϕ which is explained shortly.

$$
b = \frac{3 - \phi}{1 - \phi}
\tag{24}
$$

The minmod slope-limiter operator is

$$
\mathrm{minmod}[x, y] = \mathrm{sign}(x)\ \max[0, \min\{|x|, y\,\mathrm{sign}(x)\}]
\tag{25}
$$

Then, the left state at the cell interface at $m + 1/2$ and the right state at the cell interface $m - 1/2$ can be defined to be

$$
\begin{aligned}
Q^-_{m+1/2} &= Q_m + \sum_i \left(\frac{1 + \phi}{4} \widetilde{\alpha}^i_{m+1/2} + \frac{1 - \phi}{4} \widetilde{\alpha}^i_{m-1/2} \right) r^i_m \\
Q^+_{m-1/2} &= Q_m - \sum_i \left(\frac{1 + \phi}{4} \widetilde{\alpha}^i_{m-1/2} + \frac{1 - \phi}{4} \widetilde{\alpha}^i_{m+1/2} \right) r^i_m
\end{aligned}
\tag{26}
$$

where

$$
r^i_m = r^i(Q_m, (N_{m+1/2} + N_{m-1/2})/2)
\tag{27}
$$

At maxima and minima, the minmod operator returns a zero value and the left and right states reduce to

$$
\begin{aligned}
Q^-_{m+1/2} &= Q_m \\
Q^+_{m-1/2} &= Q_m
\end{aligned}
\tag{28}
$$

which result in a first-order accurate scheme locally.

More details on this Euler solver can be found in Refs. 12-14. Now some results are presented to illustrate the unified Euler solver capability.

Euler Results

Supersonic Flows — Figure 12a shows an elliptic waverider geometry typical of hypersonic configurations. Typically, waveriders are designed to have a lift–producing lower surface with a freestream aligned upper surface. Figure 12b shows Mach number contours at different Mach numbers and angles of attack. At the design point ($M_\infty = 4$, $\alpha = 0°$), the shock is at the leading edge while at off–design flow conditions the shock moves away from the leading edge. The upwind, TVD based Euler solver implemented in the code does not exhibit any numerical instability problems in capturing strong shocks. Figures 12c and 12d show comparisons of surface pressures and pitching moment coefficients with experimental data[30] and other available methods[31]. The full potential method compares well with the Euler results when the shock is weak. The shock strength starts to become more pronounced for $M_\infty > 4$, $\alpha \geq 5°$ as indicated by the deviation of the isentropic full potential results from the correct Euler solutions.
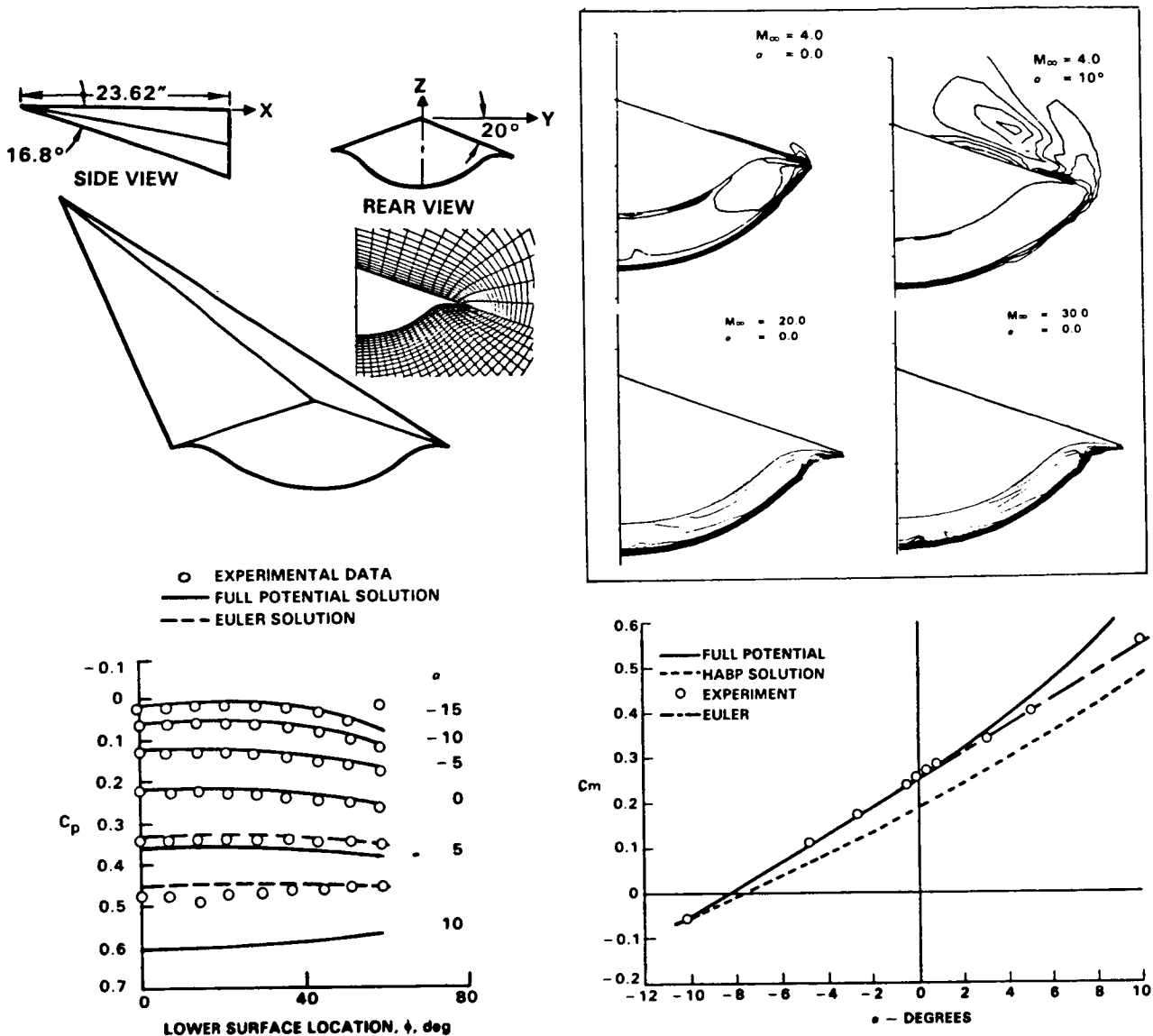
Fig. 12. Euler results for a waverider configuration; a) ge-
ometry and gridding, b) Mach contours at differ-
ent Mach numbers, c) lower surface pressures,
and d) pitching moment correlation.

Multizone Computation — For treatment of complex three-
dimensional multibody flows, the gasdynamic solvers are
provided with a multizonal capability where the physical
domain of interest is subdivided into multizones requiring
single gridding procedures within each zone. Across the
zonal boundaries proper flux balancing is maintained to
avoid spurious numerical errors originating at the interface.
The zonal interface can be permeable or impermeable and
can also be a boundary of flow discontinuity such as a shock
or sonic surface.

Figure 13 shows the Space Shuttle mated configuration
with the Orbiter mounted on top of the External Tank and
the Solid Rocket Boosters. A single zone gridding that
can treat every component of this multibody as a constant
coordinate surface, though possible, can be cumbersome
to construct. A five-zone gridding in the axial plane is
generated to study this multibody problem at supersonic
Mach numbers. Pressure contours and gridding are shown
at different marching stations for $M_\infty = 1.8$, $\alpha = 0°$. The
presence of a shock around the Shuttle OMS pod (station
C) is clear.

Transonic Flow — Figure 14 shows transonic results for the
ONERA-M6 wing. The double shock pattern on the upper
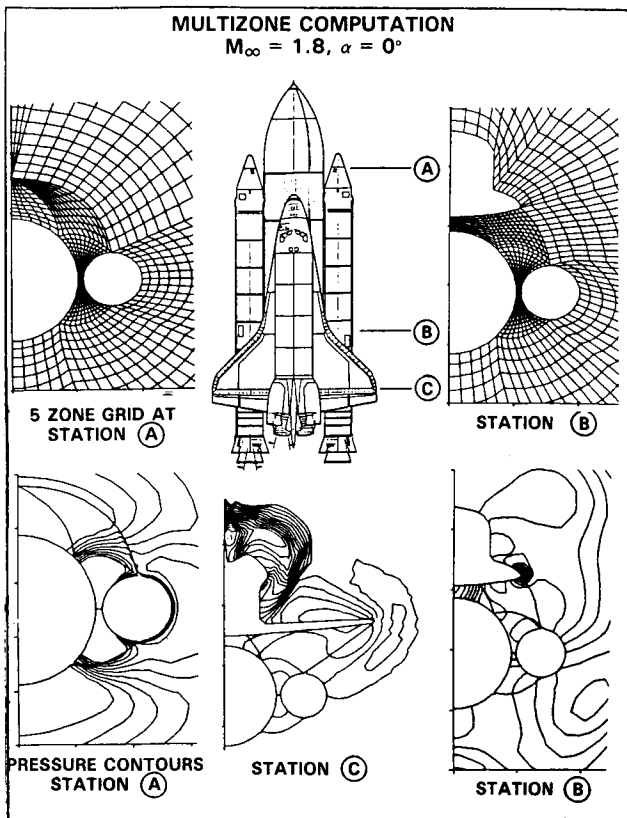surface at $M_\infty = 0.84$, $\alpha = 3.06°$ is well captured by the
Euler code.

Fig. 13. Multizone treatment of the Shuttle mated con-
figuration; $M_\infty = 1.8$, $\alpha = 0°$.

Navier-Stokes Equations

The purpose in developing powerful, robust and effi-
cient Euler solvers is not just to study inviscid strongly
shocked, rotational flows, but also to use them as a step-
ping stone in devising Navier-Stokes methods for solving
viscous flow problems. Many problems of real interest in
advanced aerospace and configuration development do re-
quire the use of Navier-Stokes methods. Some of the flows
that can only be modeled using the Navier-Stokes equations
are:

1) attached flows with a) tip vortex, b) wing/body junc-
   tion vortex, and c) cross-flow leading edge vortex;

2) separated flows (leading edge separation and shock-
   boundary layer separation);

3) acoustics/unsteady phenomena (cavity flow and inter-
   nal flow-induced vibrations);

4) high Mach number flows with significant heating; and

5) reacting flows (combustion involving chemical kinet-
   ics).

Referring to eq. (1), the Reynolds-averaged form of the
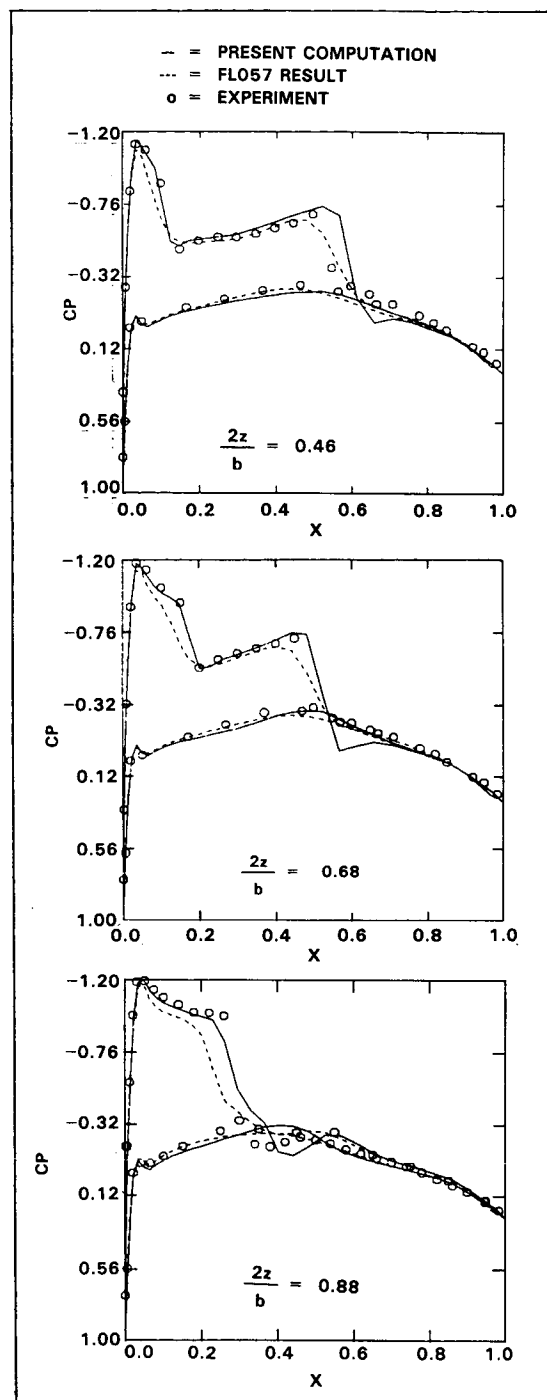Navier-Stokes equations is represented by

Fig. 14. Transonic results for the ONERA–M6 wing;
$M_\infty = 0.84$, $\alpha = 3.06°$.

$$Q = \begin{pmatrix} e \\ \rho \\ \rho u \\ \rho v \\ \rho w \end{pmatrix} ; E = E_{in} + E_v; F = F_{in} + F_v; G = G_{in} + G_v$$

(29)

where E_{in}, F_{in}, and G_{in} are the inviscid Euler fluxes given
by eq. (16) and the viscous fluxes E_v, F_v, and G_v are given
by

97

$$E_v = \frac{1}{Re} \begin{pmatrix} \frac{\gamma}{Pr}\kappa\frac{\partial T}{\partial x} + u\tau_{xx} + v\tau_{xy} + w\tau_{xz} \\ 0 \\ \tau_{xx} \\ \tau_{xy} \\ \tau_{xz} \end{pmatrix},$$

$$F_v = \frac{1}{Re} \begin{pmatrix} \frac{\gamma}{Pr}\kappa\frac{\partial T}{\partial y} + u\tau_{yx} + v\tau_{yy} + w\tau_{yz} \\ 0 \\ \tau_{yx} \\ \tau_{yy} \\ \tau_{yz} \end{pmatrix}, \qquad (30)$$

$$G_v = \frac{1}{Re} \begin{pmatrix} \frac{\gamma}{Pr}\kappa\frac{\partial T}{\partial z} + u\tau_{zx} + v\tau_{zy} + w\tau_{zz} \\ 0 \\ \tau_{zx} \\ \tau_{zy} \\ \tau_{zz} \end{pmatrix}.$$

Here, Re is the Reynolds number, Pr is the Prandtl number, κ is the thermal conductivity, and T is the specific internal energy given by $T = p/[(\gamma-1)\rho]$. The terms τ_{xx}, τ_{xy}, τ_{xz}, τ_{yx}, τ_{yy}, τ_{yz}, τ_{zx}, τ_{zy}, and τ_{zz} are given by

$$
\begin{aligned}
\tau_{xx} &= 2\mu\frac{\partial u}{\partial x} - \frac{2}{3}\mu\Phi, \\
\tau_{yy} &= 2\mu\frac{\partial v}{\partial y} - \frac{2}{3}\mu\Phi, \\
\tau_{zz} &= 2\mu\frac{\partial w}{\partial z} - \frac{2}{3}\mu\Phi, \\
\tau_{xy} = \tau_{yx} &= \mu\left(\frac{\partial u}{\partial y} + \frac{\partial v}{\partial x}\right), \\
\tau_{xz} = \tau_{zx} &= \mu\left(\frac{\partial u}{\partial z} + \frac{\partial w}{\partial x}\right), \\
\tau_{yz} = \tau_{zy} &= \mu\left(\frac{\partial w}{\partial y} + \frac{\partial v}{\partial z}\right)
\end{aligned}
\qquad (31)
$$

where

$$\Phi = \left(\frac{\partial u}{\partial x} + \frac{\partial v}{\partial y} + \frac{\partial w}{\partial z}\right)$$

and μ is the coefficient of viscosity.

The viscosity coefficient for turbulent flows is modeled as the sum of the laminar and turbulent viscosities in the eddy viscosity approach. The turbulent eddy viscosity is usually computed using one of two popular techniques, 1) by using the Baldwin-Lomax or other algebraic eddy viscosity formulation, and 2) by using a two-equation model such as the $k - \epsilon$ formulation.

The k-ϵ model often used is the standard high Reynolds number form of the equations. Even though the k-ϵ model can take more time to solve than the simpler algebraic eddy viscosity models this is justifiable since the k-ϵ model is generally applicable to a much wider class of flows. The kinetic energy equation is derived from the Navier-Stokes equations with the main limiting criterion being that it assumes local isotropy. The dissipation equation is not exact but is modelled to represent physical processes similar to those of the kinetic energy equation. Even with these assumptions the k-ϵ equations have a proven capability of adequately predicting a large range of complex flows, including anisotropic ones.

The k-ϵ equations may be solved using the same upwind, TVD formulations applied to the Euler and Navier-Stokes equations. Referring to eq. (1), the k-ϵ equations can be written as

$$Q = \begin{pmatrix} \rho k \\ \rho\epsilon \end{pmatrix}, \quad E = \begin{pmatrix} \rho u k - \frac{\mu_k}{Re}\frac{\partial k}{\partial x} \\ \rho u\epsilon - \frac{\mu_\epsilon}{Re}\frac{\partial \epsilon}{\partial x} \end{pmatrix},$$

$$C = \begin{pmatrix} \rho v k - \frac{\mu_k}{Re}\frac{\partial k}{\partial y} \\ \rho v\epsilon - \frac{\mu_\epsilon}{Re}\frac{\partial \epsilon}{\partial y} \end{pmatrix}, \quad D = \begin{pmatrix} \rho w k - \frac{\mu_k}{Re}\frac{\partial k}{\partial z} \\ \rho w\epsilon - \frac{\mu_\epsilon}{Re}\frac{\partial \epsilon}{\partial z} \end{pmatrix}. \qquad (32)$$

The only exception is that the k-ϵ equations, in addition to the above, involve a source term on the right hand side given by

$$S = \frac{1}{Re}\begin{pmatrix} P - \rho\epsilon Re \\ C_1\frac{\epsilon}{k}P - C_2\rho\frac{\epsilon^2}{k}Re \end{pmatrix}. \qquad (33)$$

In eqs. (31) and (32),

$$\mu_k = (\mu + \mu_t/\sigma_k)$$
$$\mu_\epsilon = (\mu + \mu_t/\sigma_\epsilon)$$

k is kinetic energy, ϵ is turbulent dissipation, and μ_t is turbulent eddy viscosity. P represents the production of kinetic energy and the following simplified form of it is used

$$P = \mu_t(u_x^2 + u_y^2 + u_z^2). \qquad (34)$$

The k-ϵ model still employs the eddy viscosity/diffusivity concept as it relates eddy viscosity to the kinetic energy and dissipation by

$$\mu_t = C_\mu\rho\frac{k^2}{\epsilon}. \qquad (35)$$

This eddy viscosity is then used to create an effective viscosity $(\mu + \mu_t)$ which replaces μ in the Reynolds-averaged Navier-Stokes equations. To solve the above turbulence model the following constants must be specified: $\sigma_k = 1.0$, $\sigma_\epsilon = 1.3$, $C_1 = 1.44$, $C_2 = 1.92$, and $C_\mu = 0.09$.

One of the highlights of the Navier–Stokes activity is the modeling of turbulence for separated flows. The new turbulence model is based on experimental observations of separated turbulent flows. The model prescribes turbulence kinetic energy (k) and its dissipation (ϵ) analytically inside separation bubbles. A Gaussian variation of k normal to walls is assumed. The length scale of turbulence within bubbles is proportional to the local distance from the wall to the edge of the viscous sublayer, which is located outside the backflow region, as shown in figure 15. The latter feature is a basic assumption of the model.

The stress scale is the local maximum Reynolds stress, which typically occurs around the middle of the boundary layer, well outside the bubble. This scale must be supplied by the turbulence model used beyond separated regions.

The main equations of the model are given in Ref. 23. A simple formula for eddy viscosity distribution within the separation bubble results, and is used to provide eddy viscosity for the Reynolds-averaged equations when performing the calculations inside the bubble. Outside of it, another turbulence model (e.g., Baldwin–Lomax or k-ϵ) supplies the values of eddy viscosity.
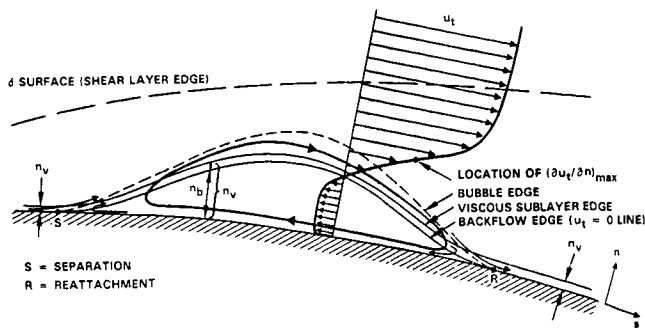
98

Fig. 15. Schematic view of separated flow bubble and basic nomenclature.

Navier–Stokes Results

The algebraic k-ϵ turbulence model for separated flows, in conjunction with the Baldwin–Lomax model, has been incorporated into a finite volume, time–marching, multizonal Navier–Stokes code[23–26], featuring an implicit upwind–biased scheme, approximate factorization, and Total Variation Diminishing discretization for high accuracy. When a separation bubble exists, the standard Baldwin–Lomax or the k-ϵ model is used to compute eddy viscosity outside the backflow region, while the separation model (figure 15) provided eddy viscosity within the separation bubble.

Several unit problems are computed to check the validity of the Navier–Stokes code with a turbulence model for treating separated flows.

As a first computational test of the new turbulence model, a transonic flow calculation over an axisymmetric boattail with a cylindrical extension (solid plume simulator) has been performed. Figure 16a shows the chosen geometry. This case involves a moderate–sized separation bubble at the end of the boattail. The data of Ref. 32 at $M_\infty = 0.8$ and a Reynolds number of 1.8×10^6, based on maximum model diameter, were used for comparisons with the calculations. A 65×40 grid was employed, with 23 points normal to the wall lying inside the separation bubble at the location of its maximum height. Figure 16b shows a detail of the computational mesh.

In figure 16c, pressure coefficient at the wall, calculated using the new separation turbulence model, is compared with experimental data of Ref. 32 as well as with a calculation which used the Baldwin–Lomax model by itself. The figure also indicates the location and extent of the separated region. The advantage of using the separation model is demonstrated by the significant improvement in predicting the pressure through the separated zone, compared to the corresponding calculation without the model.

Figure 16d compares skin friction distribution, as calculated using the new model, with the corresponding calculation done without it. A larger separation bubble is predicted by the former. No data are available for comparison.
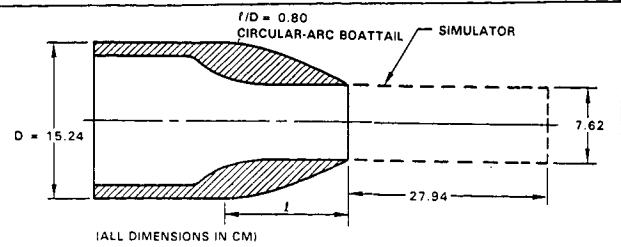
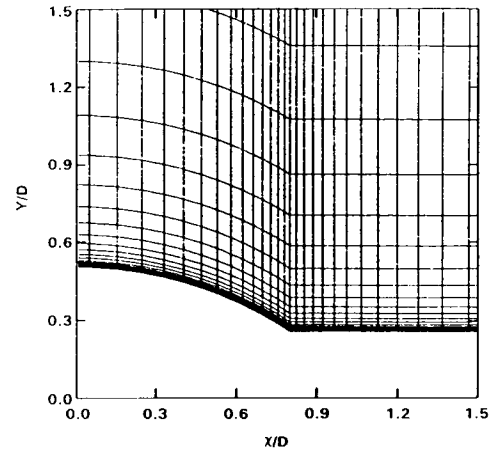

Fig. 16a. Sketch of boattail with solid plume simulator.

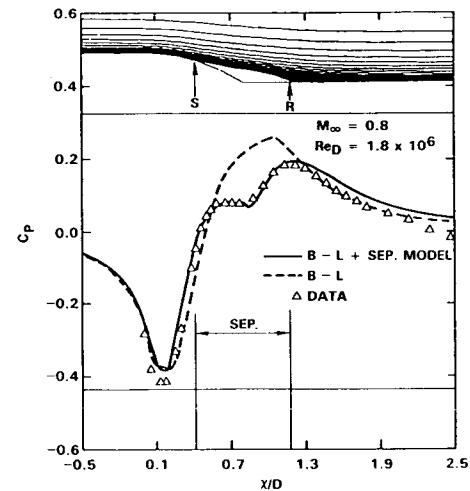

Fig. 16b. Computational grid for the solid plume.

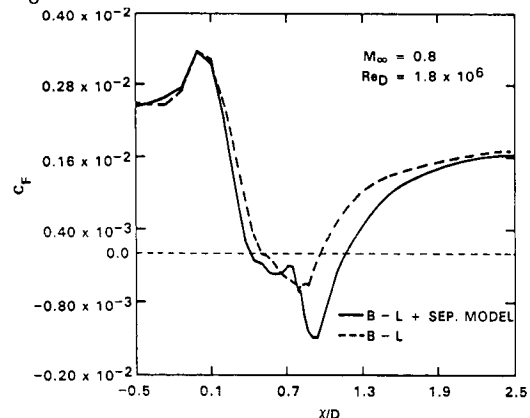Fig. 16c. Boattail streamwise wall–pressure distribution.

Fig. 16d. Boattail streamwise skin friction distribution.

The second test of the separation model was chosen to be a supersonic flow over a 24° compression ramp. Detailed experimental data are available for this case[33-35], which involves a rather large separated flow region. The 65 × 35 grid used for the calculations is shown in figure 17a. About 75% of the normal-to-wall mesh points were located within the shear layer. This case was run at $M_\infty = 2.85$ and a Reynolds number based on incoming boundary layer thickness of 1.6×10^6.

Figure 17b shows a comparison between calculations and experimental data of wall pressure distribution. The improved predictional capability due to inclusion of the separation model is evident.

Figure 17c compares calculations with experimental data of skin friction. The advantage of using the separation model over the regular Baldwin-Lomax model is evident throughout the separation bubble. Incorporation of the new model enables precise prediction of reattachment location, a difficult task for this flow.

A streamline plot, resulting from the calculation with the separation model, is shown in figure 17d. The predicted extent of the separated region agrees quite well with the experimentally observed locations of separation and reattachment, also indicated in the figure.

The third test of the new backflow model was the backward-facing step case reported in Ref. 36, with an inflow Mach number of 0.128 and a Reynolds number of 31,250 based on inflow conditions and the step height as a reference length.

Figure 18a shows the geometry and the two-zone computational grid, with a 42 × 22 mesh used in the subdomain above the step, and a 36 × 20 mesh used in the subdomain downstream of the step.

Pressure distribution along the step-side wall is shown in figure 18b, as resulting from the current approach and from Sindir's[37] calculations using the $k-\epsilon$ model. Comparison with the data indicates a slight advantage in using the new algebraic model over the $k-\epsilon$ model.

Figure 18c shows skin friction distribution on the step-side wall. The new backflow model enables improved prediction and significantly better performance in the reattachment zone. In the vicinity of the step corner, the skin friction is positive, indicating a small counter-rotating vortex, in agreement with the data.

In figure 18d, streamwise velocity profiles at two locations are shown, one upstream of the reattachment region, the other downstream of it. Agreement with the data is very good at the former location, where the flow is separated, and fair at the latter, where a somewhat sluggish boundary layer recovery is predicted for the lower part of the profile.

Figure 18e shows Reynolds stress profiles at the locations corresponding to those of figure 18d. While the shape of the calculated profile agrees with the experimental one at the upstream location, the magnitude is overpredicted roughly by a factor of two. In the downstream location, however, agreement with data is quite good, although the lower part of the calculated profile is again overpredicted.
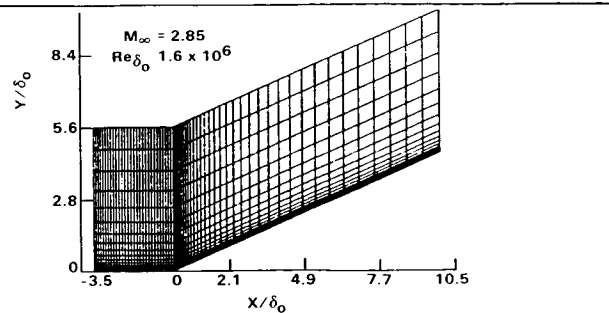

Fig. 17a. Computational grid for the 24° compression ramp.
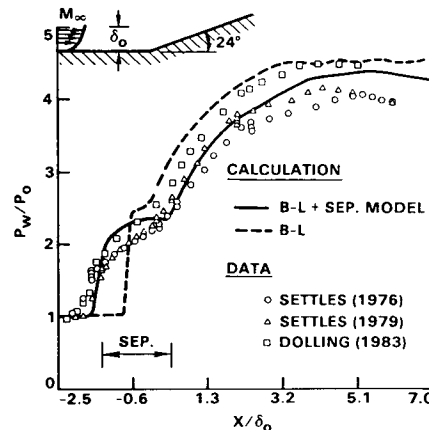

Fig. 17b. Streamwise wall-pressure distribution over ramp.
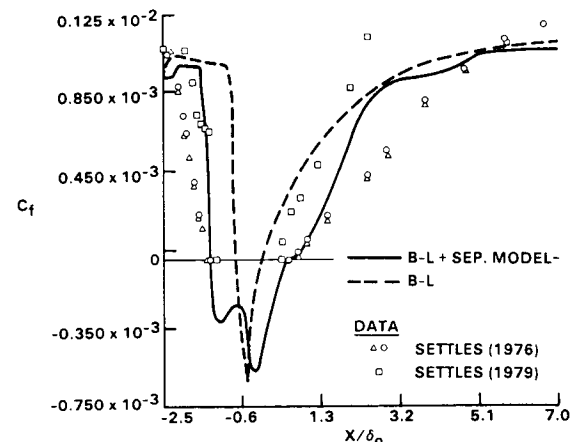

Fig. 17c. Streamwise skin friction distribution over ramp.
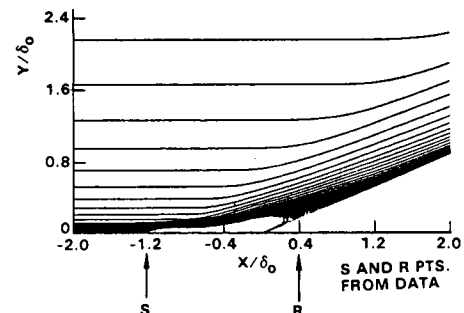

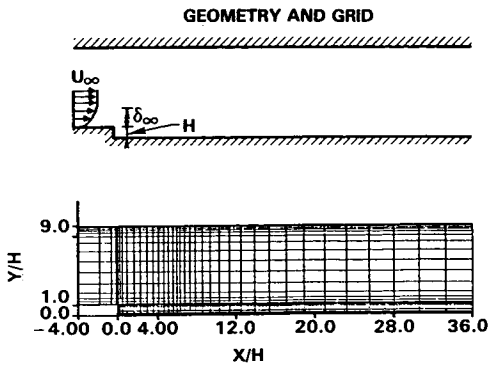Fig. 17d. Ramp streamline plot, showing the separation bubble.

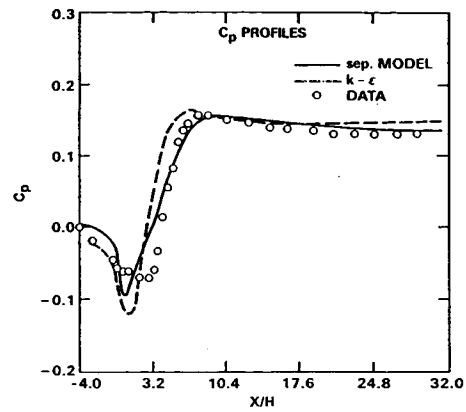Fig. 18a. Two-zone computational grid and geometry for backward-facing step.

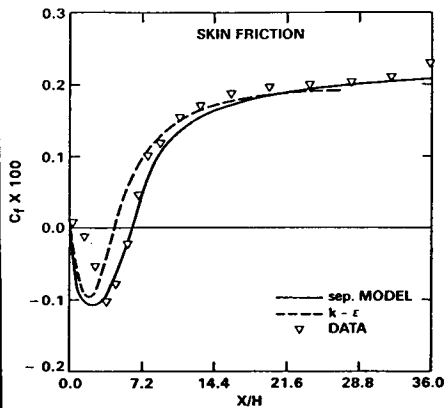Fig. 18b. Step-side pressure distribution.
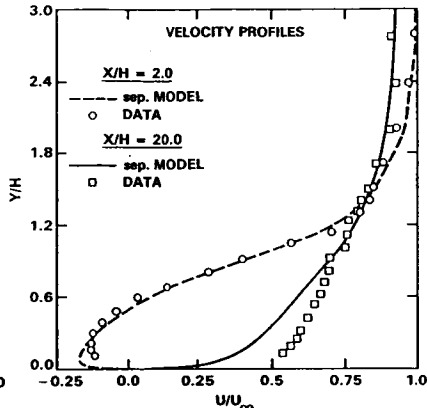
Fig. 18c. Step-side skin friction distribution.

Fig. 18d. Streamwise velocity profiles upstream and down-stream of reattachment.
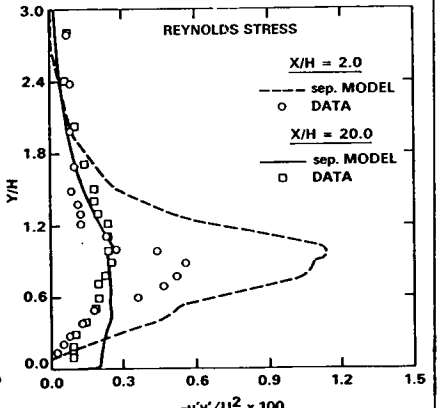
Fig. 18e. Reynolds stress profiles

Since store separation and aerodynamic drag due to open cavities are important issues in design, cavity computations are vital for validation and prediction. A laminar three-dimensional cavity computation has been done. The specific cavity is a simplified version of the F-111 weapons bay. Figure 19a shows velocity directions down the center-line of the cavity. Figure 19b shows the velocity directions of the secondary motion on a cross plane of the cavity. More cavity results can be found in Ref. 38.

Fig. 19. F-111 cavity flow; a) center plane, b) cross plane.

Fig. 20a. Test case geometry.

Fig. 20b. Computational grid

Fig. 20c. Pressure contours

Fig. 20d. Wall pressure comparison

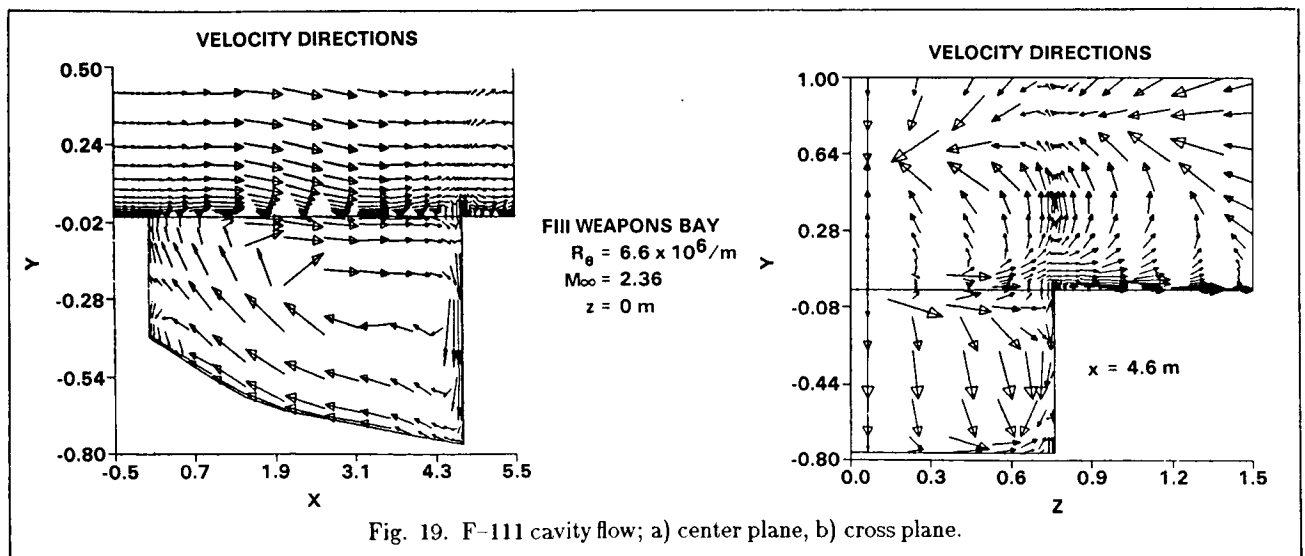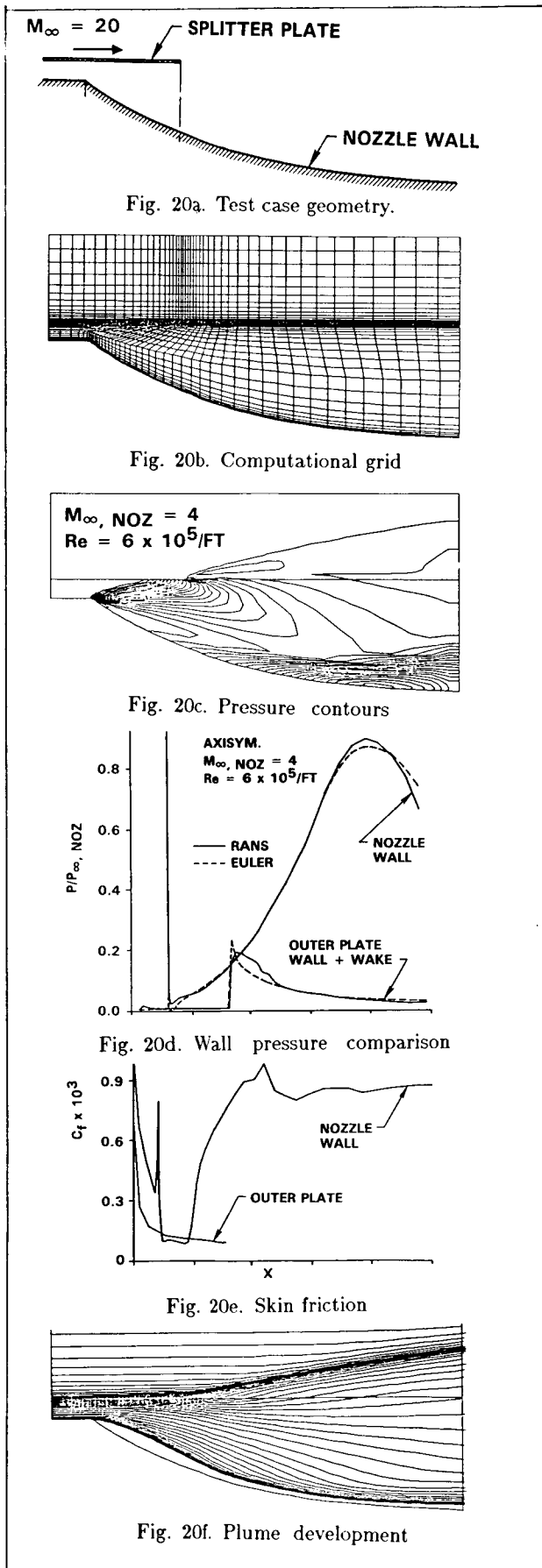Fig. 20e. Skin friction

Fig. 20f. Plume development

Figure 20a shows an axisymmetric nozzle and the corresponding two-zone gridding is given in figure 20b. The external inflow was fixed at $M_\infty = 20$, while the nozzle inflow Mach number was varied from 4.0 to 1.5. The nozzle inflow pressure was 217 times that of the external inflow. For the viscous calculations, the Reynolds number based on nozzle inflow conditions was varied from 6×10^5/ft at Mach 4 to 2.25×10^5/ft at Mach 1.5. All solid surfaces were held at a constant wall temperature $T_W = 0.34 T_{\infty,noz}$. Calculations for this case were run using both the Reynolds-averaged Navier–Stokes code (RANS) and the Euler code. Figure 20c shows pressure contours for the Navier–Stokes computation. Figure 20d compares pressure distributions on the nozzle wall and on the outer plate surface plus the wake region downstream of it, as resulting from the RANS and Euler calculations. Except for the milder corner expansion due to viscous displacement effects, the two calculations predict the same nozzle wall pressure distribution. In the near wake region downstream of the splitter plate, however, the interaction between the shear layers from both sides of the plate and the plume–induced shock/boundary layer interaction in the vicinity of the plate trailing edge modify the pressure distribution as compared with the inviscid prediction. Further downstream the two predictions coincide. Figure 20e shows skin friction on the two walls, indicating no separation of the boundary layers. The streamline plot in figure 20f shows the plume development as predicted by the RANS code.

Figure 21a shows the geometry and the multizone gridding for a ramjet configuration. Figure 21b shows viscous Mach number contours for an inflow Mach number of 4.03.

The Navier–Stokes code developed at the Rockwell Science Center is still undergoing validation tests on several unit problems for possible improvements in modeling turbulence of separated flows. Future applications will involve wings, wing–body combinations at high α, and cavity–store acoustics and separation studies.

Fig. 21a. Geometry and gridding for a ramjet.

Fig. 21b. Mach contours, $M_\infty = 4.03$.
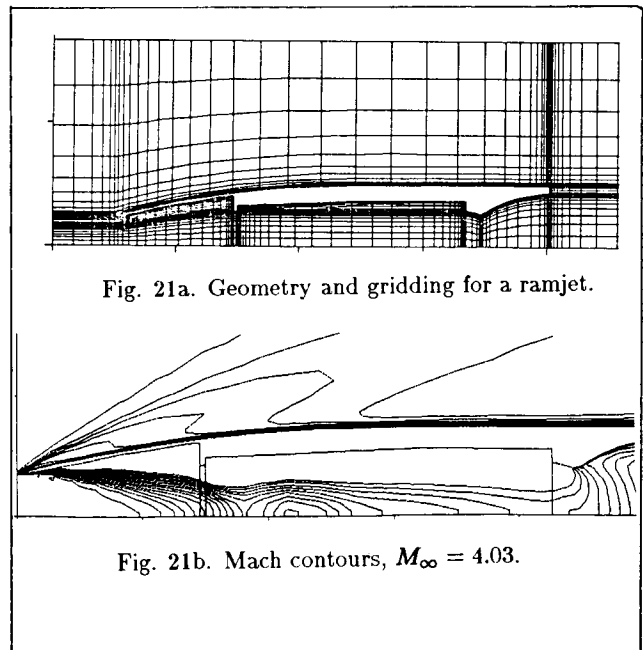
Laser–Material Interaction

The paper so far dealt with the development and application of computational algorithms for solving aerodynamic problems. Extension of these CFD methods to solving problems in other disciplines that are governed by an appropriate set of partial differential equations is very attractive. One such application is to study the problem of heat transfer in materials subjected to intense laser heating.

Laser heat treatment of materials (especially iron–base alloys and carbon–carbon composites) for various industrial applications is becoming very attractive due to ease in the controllability and in generation of laser beams. For example, use of laser as a heat source in enhancing materials resistance to surface wear and corrosion through solid state phase transformations (without melting) and rapid solidification (with shallow melting), in achieving a desired homogeneous molten weld pool, and in obtaining a unique surface composition through coating or cladding, as a viable economical process, has been well proven in laboratory settings. Transitioning this process technology from a laboratory setting to an industrial environment requires a better understanding of the role of various controlling parameters, such as the cross–section of the laser, power intensity of the laser, velocity of the moving laser or the workpiece, and the material properties themselves in determining the quality of the surface modification process. Optimization of these controlling process parameters through theoretical modeling and computational simulation can lead to achieving the desired properties of surface treatment.

Figure 22 shows the schematic of a laser melted material pool. When the workpiece is swept under the beam, a self quenched heat treated zone is obtained along the surface. Dimensions of the melted zone $(T > T_m$, where T_m is the melting temperature) and the heat affected zone $(T > T_c)$ are controlled by absorbed laser beam power density, beam size, and travel speed.

MZ - MELTED ZONE
HAZ - HEAT AFFECTED ZONE
T_c - PHASE TRANSFORMATION TEMP.
T_m - MELTING TEMP.

• SURFACE TENSION DRIVEN
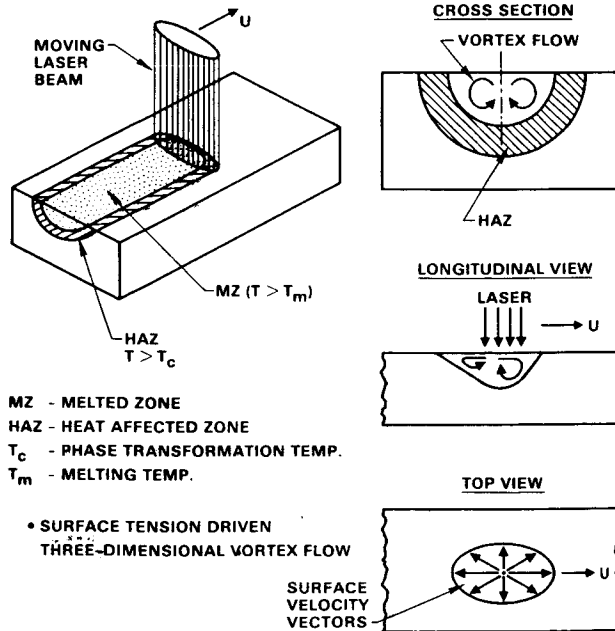THREE–DIMENSIONAL VORTEX FLOW

Fig. 22. Surface tension induced convective heat transfer.

The high surface temperature gradients in the melted zone create a variation of surface tension along the surface which is balanced by shear forces. This balancing shear force is created by setting up a counter rotating vortex flow within the molten zone as described in figure 22.

The physics of modeling the heat transfer process occurring in figure 22 involves both conduction and convection in a high gradient thermal field. The equation that best describes the physical phenomena of this problem is the incompressible Navier–Stokes equations. Referring to eq. (3), the following describes the coupling between the temperature field and the velocity field.

$$Q = \left\{ \begin{array}{c} 0 \\ \rho u \\ \rho v \\ \rho w \\ T \end{array} \right\} \; ; \; E = \left\{ \begin{array}{c} u \\ p + \rho u^2 - \tau_{xx} \\ \rho uv - \tau_{xy} \\ \rho uw - \tau_{xz} \\ Tu - \alpha \frac{\partial T}{\partial x} \end{array} \right\} \; ;$$

$$F = \left\{ \begin{array}{c} v \\ \rho uv - \tau_{xy} \\ p + \rho v^2 - \tau_{yy} \\ \rho vw - \tau_{yz} \\ Tv - \alpha \frac{\partial T}{\partial y} \end{array} \right\} \; ; G = \left\{ \begin{array}{c} w \\ \rho uw - \tau_{xz} \\ \rho vw - \tau_{yz} \\ p + \rho w^2 - \tau_{zz} \\ Tw - \alpha \frac{\partial T}{\partial z} \end{array} \right\} \; ; \tag{36}$$

$$\alpha = \frac{k}{\rho c_p}$$

where $\tau_{ij} = \nu \left(\frac{\partial u_i}{\partial x_j} + \frac{\partial u_j}{\partial x_i} \right)$. Modeling of turbulence in τ_{ij} is neglected in the present formulation and only the laminar stress tensor is considered.

In these equations, c_p is the specific heat, ρ is the density, k is the thermal conductivity, T is the temperature, and ν is the kinematic viscosity. The induced velocity field in the molten pool is represented by u_j.

In the unmelted region of the material where the heat transfer process is purely due to conduction (temperatures below melting), only the energy equation needs to be solved for temperature (see Ref. 39).

On the outer surface of the molten pool, the force balance equations are

$$\mu \frac{\partial u}{\partial z} = \sigma' \frac{\partial T}{\partial x}$$
$$\mu \frac{\partial v}{\partial z} = \sigma' \frac{\partial T}{\partial y} \tag{37}$$

where σ' is the rate of change of surface tension $(N/m/k)$ with temperature and μ is the coefficient of viscosity of the molten pool (N sec/m^2; N is Newton).

At the liquid–solid interface $u = v = w = 0$ and $T = T_m$. More details on the boundary condition can be found in Ref. 40.

The computational method employs an implicit triple approximate factorization scheme to solve the energy equation in terms of temperature and an explicit treatment for the three momentum equations and the continuity equation. The pressure field is updated at each time level using a Poisson solver to satisfy the continuity equation.

Laser Results

A sample result for a rectangular workpiece undergoing melting is presented.

Figure 23 shows results for a typical case (5000 W laser, 4 × 3 mm laser cross section, 1.26 mm/sec beam travel speed). A point in the workpiece is considered heat affected if that point experienced temperatures above 750°C and the melt zone corresponds to temperatures $\geq 1500°C$. At a given instance of time (laser beam around the halfway length of the workpiece), the instantaneous temperature distribution, melt zone shape, and the three–dimensional vortex mixing material flow are shown in the figure. The cross–sectional view, longitudinal view (plane of symmetry), and the top view of the melted zone clearly reveal the convection process induced by the surface tension driven flow. Pure conduction treatment of this heat transfer problem (no convection model, i.e., surface tension gradients set to zero) results in temperature levels not comparable with experimental observations. The computational procedure of the present study incorporating the surface tension driven convective heat transfer process produces melt zone and heat affected zone shapes very similar to experimental data. More results are presented in Ref. 40.

Application of this work to study problems of deep welding (solute redistribution, microstructure of the heat affected zone, and residual stress state) and characterization of the surface ripples are some of the ongoing projects.

Electromagnetic Scattering

The objective is to develop time–dependent finite difference methods to solve the Maxwell equations to study the problem of electromagnetic scattering from dielectric and perfectly reflecting objects. Although techniques based on the integral form of the equations are available, they are usually restricted in their application due to various simplifications made in the formulation. Solution techniques to the differential equation usually provide a general–purpose capability with fewer restrictions than techniques based on the integral approach. Based on proven CFD methods, it is desirable to develop an efficient finite difference technique for the Maxwell equations.

Referring to eq. (1), the Maxwell equations take the form

$$Q = \left\{ \begin{array}{c} e_x \\ e_y \\ e_z \\ H_x \\ H_y \\ H_z \end{array} \right\} \; ; \; E = \left\{ \begin{array}{c} 0 \\ -\frac{1}{\mu}e_z \\ \frac{1}{\mu}e_y \\ 0 \\ \frac{1}{\epsilon}H_z \\ -\frac{1}{\epsilon}H_y \end{array} \right\} \; ;$$

$$F = \left\{ \begin{array}{c} \frac{1}{\mu}e_z \\ 0 \\ -\frac{1}{\mu}e_x \\ -\frac{1}{\epsilon}H_z \\ 0 \\ \frac{1}{\epsilon}H_x \end{array} \right\} \; ; \; G = \left\{ \begin{array}{c} -\frac{1}{\mu}e_y \\ \frac{1}{\mu}e_x \\ 0 \\ \frac{1}{\epsilon}H_y \\ -\frac{1}{\epsilon}H_x \\ 0 \end{array} \right\} \tag{38}$$
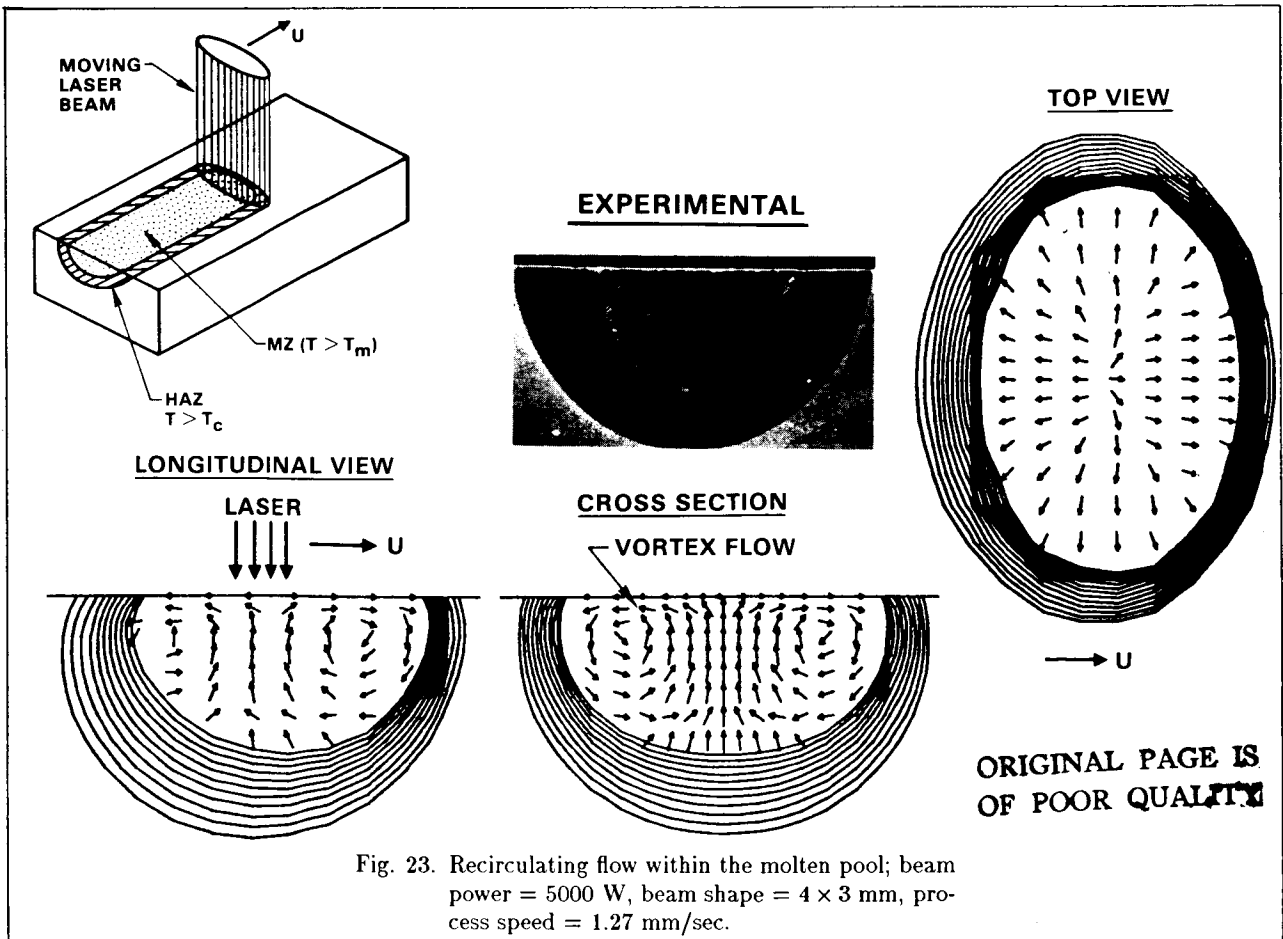
Fig. 23. Recirculating flow within the molten pool; beam power = 5000 W, beam shape = 4 × 3 mm, process speed = 1.27 mm/sec.

where e_x, e_y, and e_z are the electric field components along x, y, and z, and similarly H_x, H_y, and H_z are the magnetic field components. The parameters ϵ, μ, and σ represent permittivity, permeability, and conductivity of the medium through which the electromagnetic wave is propagating. Equation (38) is hyperbolic and has real eigenvalues and a linearly independent set of eigenvectors. Upwind schemes developed for the Euler equations are ideal for solving the Maxwell equations. The objective is to solve eq. (3) subject to an incident wave to compute the equivalent surface current on the object given by $n \times H$ where n is the surface normal and H is the magnetic field vector. Once the equivalent surface current is known on the dielectric object and around any contour encompassing the object, the radar cross section (RCS) information can be obtained using a near field-to-far field transformation (Refs. 41,42). The RCS information depends on the intensity of the scattered wave.

RCS Results

The Maxwell equations in two dimensions can be specialized for a transverse magnetic (TM) wave ($e_x = e_y = 0, H_z = 0$), or for a transverse electric (TE) wave ($H_x = H_y = 0, e_z = 0$). Development of computational algorithms for studying electromagnetic scattering from perfectly conducting or dielectric objects can benefit from solving the TM or the TE wave problem. Preliminary results are reported here for the electromagnetic scattering from a perfectly conducting square cylinder for an incident plane wave of the form $e_i = e_0 \sin k(r \cos(\phi - \phi') - ct)$ where e_0 is the amplitude, $k = 2\pi/\lambda$, λ is the wavelength, c is the wave speed, ϕ' is the angle of incident wave with respect to the x-axis. Figures 24a and 24b show the surface current $J_z = n \times H$ on the cylinder for two different incident wave angles. The correlation of $n \times H$ obtained using a simple, first-order accurate, upwind, explicit scheme with an existing method known as method of moments (MOM) is good. Knowing this J_z information, the RCS value for different viewing angles can be computed. Development of higher order accurate, upwind schemes based on Euler solvers is currently in progress. Some of the numerical issues to be addressed in this development are 1) higher order accurate nonreflecting farfield conditions based on characteristic theory, 2) grid resolution requirements for high frequency (small λ or large k) incident waves, 3) boundary condition treatment for radar absorbing materials taking into account frequency dependence on ϵ, μ and σ, 4) multizone gridding techniques for interior and external regions, and 5) near-field to far-field transformations to derive RCS values from the near-field $n \times H$ and $n \times E$ information.
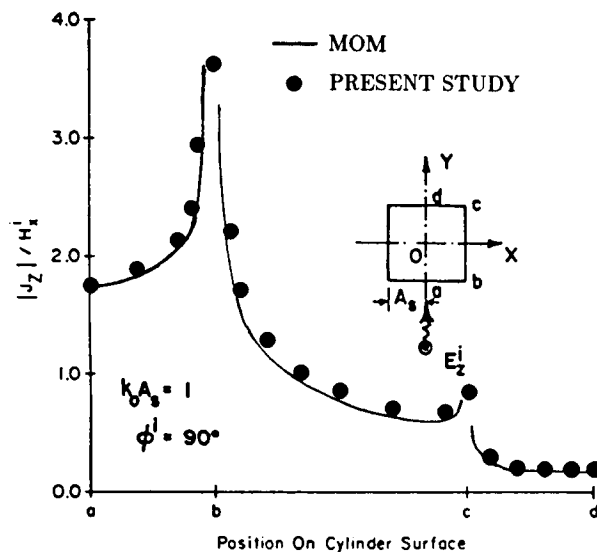

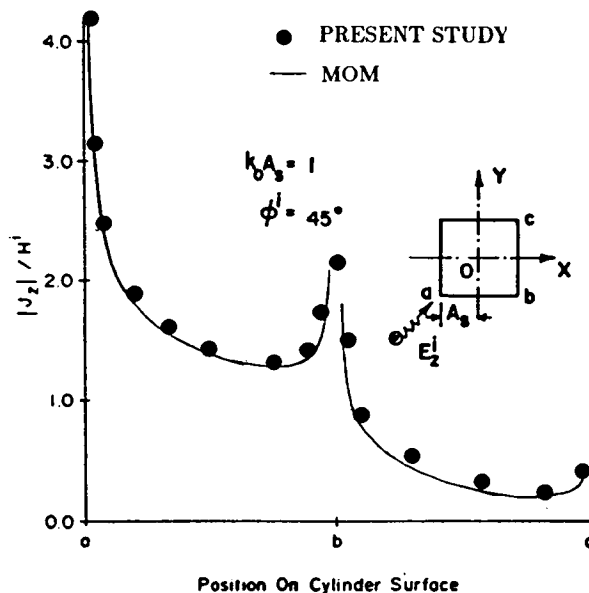Fig. 24a Surface current on a square cylinder for a right moving incident wave.

Fig. 24b Surface current on a square cylinder for an incident wave at 45°.

CONCLUSIONS

The state of the art of Computational Fluid Dynamics has taken rapid strides in recent years with the development and application of unified, robust, and efficient methods. The advances in CFD are also beginning to make a positive impact on other areas of mathematical science, leading to the emergence of the concept of "Computational Science". In this new spirit, this paper has presented a unification of algorithms and their application to fluid dynamics, electromagnetics, and material characterization.

REFERENCES

1. Gingrich, P.B., Child, R.D., and Panageas, G.N., "Aerodynamic Development of the Highly Maneuverable Aircraft Technology Remotely Piloted Research Vehicle," NASA CR-143841, June 1977.

2. Bonner, E. and Gingrich, P.B., "Transonic Computational Experience for Advanced Tactical Aircraft," *Progress in Astronautics and Aeronautics*, Vol. 81, Transonic Aerodynamics, D. Nixon, editor, American Institute of Aeronautics and Astronautics, 1982.

3. Gingrich, P.B. and Bonner, E., "Wing Design for Supersonic Cruise/Transonic Maneuver Aircraft," 13th Council of the International Council of Aeronautical Sciences, Vol. 2, American Institute of Aeronautics and Astronautics, August 1982.

4. Bonner, E. and Gingrich, P.B., "Supersonic Cruise/Transonic Maneuver Wing Section Development," Air Force Flight Dynamics Laboratory Report AFAWL-TR-80-3047, June 1980.

5. Bonner, E., Clever, W., and Dunn, K., "Aerodynamic Preliminary Analysis System," NASA CR-145284, April 1978.

6. Clever, W.C., "Supersonic Second Order Analysis and Optimization Program," NASA CR-172342, August 1984.

7. Shankar, V., Ide, H., Gorski, J., and Osher, S., "A Fast, Time-Accurate Unsteady Full Potential Scheme," AIAA Paper No. 85-1512-CP, AIAA 6th Computational Fluid Dynamics Conference, Cincinnati, July 15-17, 1985.

8. Shankar, V., "Treatment of Steady and Unsteady Flows Using a Fast, Time-Accurate Full Potential Scheme," AIAA Paper No. 85-4060, AIAA 3rd Applied Aerodynamics Conference, Colorado Springs, October 14-16, 1985.

9. Shankar, V. and Ide, H., "Unsteady Full Potential Computations for Complex Configurations," AIAA Paper No. 87-0110, AIAA 25th Aerospace Sciences Meeting, Reno, January 1987.

10. Caughey, D.A. and Jameson, A., "Recent Progress in Finite Volume Calculations for Wing-Fuselage Combinations," AIAA Paper No. 79-1513, July 1979.

11. Jameson, A., Baker, T.J., and Weatherhill, N.P., "Calculation of Inviscid Transonic Flow over a Complete Aircraft," AIAA Paper No. 86-0103.

12. Chakravarthy, S.R. and Szema, K.-Y., "Unified Euler Algorithms for the Euler Equations," in preparation.

13. Chakravarthy, S.R., "The Versatility and Reliability of Euler Solvers Based on High-Accuracy TVD Formulations," AIAA Paper No. 86-0243, presented at the AIAA 24th Aerospace Sciences Meeting, Reno, January 6-9, 1986.

14. Chakravarthy, S.R. and Ota, D.K., "Numerical Issues in Computing Inviscid Supersonic Flow over Conical Delta Wings," AIAA Paper No. 86-0440, presented at the AIAA 24th Aerospace Sciences Meeting, Reno, January 6-9, 1986.

15. Szema, K.-Y. and Shankar, V., "Full Potential Solutions of Three-Dimensional Complex Geometries and Multibody Configurations," AIAA Paper No. 85-0272, Reno, January 1985.

16. Shankar, V. and Osher, S., "An Efficient Full Potential Implicit Method Based on Characteristics for Analysis of Supersonic Flows," AIAA Paper No. 82-0974, June 1982; AIAA J. 21 (9), 1262 (1983).

17. Shankar, V., Szema, K.-Y., and Osher, S., "A Conservative Type-Dependent Full Potential Method for the Treatment of Supersonic Flows with Embedded Subsonic Regions," AIAA Paper No. 83-1887; AIAA J. 23 (1), 41-48 (1985).

18. Szema, K.-Y. and Shankar, V., "Nonlinear Computation of Wing-Body-Vertical Tail-Wake Flows at Low Supersonic Speeds," AIAA Paper No. 84-0427.

19. Shankar, V., "A Unified Full Potential Scheme for Subsonic, Transonic, and Supersonic Flows," AIAA Paper No. 85-1643, AIAA 18th Fluid Dynamics, Plasmadynamics, and Lasers Conference, Cincinnati, July 16-18, 1985.

20. Chakravarthy, S.R. and Szema, K.-Y., "An Euler Solver for Three-Dimensional Supersonic Flows with Subsonic Pockets," AIAA Paper No. 85-1703, presented at the AIAA 18th Fluid Dynamics, Plasmadynamics, and Lasers Conference, Cincinnati, July 16-18, 1985.

21. Szema, K.-Y., Chakravarthy, S.R., and Dresser, H., "Multizone Euler Marching Technique for Flows over Multibody Configurations," AIAA Paper No. 87-0592, January 1987.

22. Nash, J. and Scruggs, R., "An Implicit Method for the Calculation of Three-Dimensional Boundary Layers on Finite, Thick Wings," AFFDL TR-77-122, February 1977.

23. Goldberg, U.C., "Separated Flow Treatment with a New Turbulence Model," AIAA J. 24, 1711-1713 (1986).

24. Goldberg, U.C. and Chakravarthy, S.R., "Prediction of Separated Flows with a New Turbulence Model," submitted for publication in AIAA J., Rockwell Science Center Preprint No. SC-PP-86-183.

25. Goldberg, U.C. and Chakravarthy, S.R., "Comparison Between Navier–Stokes and Euler Calculations for a Class of Supersonic Nozzle Flows," in preparation.

26. Ota, D.K., Chakravarthy, S.R., and Gorski, J.J., "Inviscid and Viscous Simulations of High Angle of Attack Flows," SAE Technical Paper Series No. 851820, presented at the Aerospace Technology Conference and Exposition, Long Beach, California, October 14–17, 1985.

27. Stratton, J.A., Electromagnetic Theory, McGraw–Hill Book Company, Inc., New York, 1941.

28. Van Roosbroeck, W., "Theory of the Flow of Electrons and Holes in Germanium and Other Semiconductors," Bell System Tech. Journal, Vol. 29, 1950, p. 560.

29. Roe, P.L., "Approximate Riemann Solvers, Parameter Vectors, and Difference Schemes," J. of Computational Physics, Vol. 43, 1981, pp. 357–372.

30. Jischke, M.C., Rasmussen, M.L., and Daniel, D.C., "Experimental Results for Surface Pressures on Cone–Derived Waveriders in the Mach Number Range 3 to 5," AIAA Paper 82-0249, presented at the AIAA 20th Aerospace Sciences Meeting, Orlando, January 1982.

31. Gentry, A.E. and Smythe, D.E., "Hypersonic Arbitrary–Body Aerodynamic Computer Program (Mark III Version)," Vol. I – User's Manual, Report DAC 61552 (available from DTIC as 851811), McDonnell Douglas Corp., April 1968.

32. Abeyounis, W.K. and Putnam, L.E., "Investigation of the Flow Field Surrounding Circular–Arc Boattail Nozzles at Subsonic Speeds," NASA TP 1633, May 1980.

33. Settles, G.S., Vas, I.E., and Bogdonoff, S.M., "Details of a Shock–Separated Turbulent Boundary Layer at a Compression Corner," AIAA J., Vol. 14, No. 12, December 1976, pp. 1709–1715.

34. Settles, G.S., Fitzpatrick, T.J., and Bogdonoff, S.M., "Detailed Study of Attached and Separated Compression Corner Flowfields in High Reynolds Number Supersonic Flow," AIAA J., Vol. 17, No. 6, June 1979, pp. 579–585.

35. Dolling, D.S. and Murphy, M.T., "Unsteadiness of the Separation Shock Wave Structure in a Supersonic Compression Ramp Flowfield," AIAA J., Vol. 21, No. 12, December 1983, pp. 1628–1634.

36. Driver, D.M. and Seegmiller, H.L., "Features of a Reattaching Turbulent Shear Layer in Divergent Channel Flow," AIAA J., Vol. 23, No. 2, February 1985, pp. 163–171.

37. Sindir, M., "Numerical Study of Separating and Reattaching Flows in a Backward–Facing Step Geometry," doctoral dissertation, Mechanical Engineering, University of California at Davis, California, 1982.

38. Gorski, J.J., Ota, D.K., Chakravarthy, S.R., and Shankar, V., "Calculation of Three–Dimensional Cavity Flowfields," AIAA Paper No. 87-0117.

39. Shankar, V. and Gnanamuthu, D., "Computational Simulation of Laser Heat Processing of Materials," AIAA Paper No. 85-0390.

40. Shankar, V. and Gnanamuthu, D., "Computational Simulation of Heat Transfer in Laser Melted Material Flow," AIAA Paper No. 86-0461.

41. Shankar, V. and Chakravarthy, S.R., "An Approach to Computational Simulation of Problems in Electromagnetic Scattering," in preparation.

42. Umashankar, K. and Taflove, A., "A Novel Method to Analyze Electromagnetic Scattering of Complex Objects," IEEE Trans. on Electromagnetic Compatibility, Vol. EMC–24, No. 4, November 1982, p. 397.